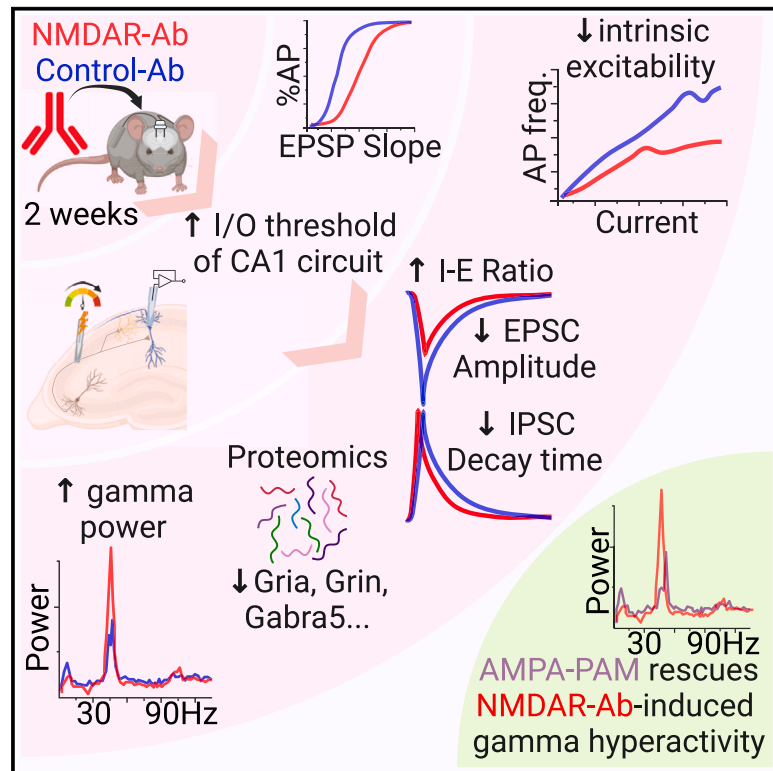# Human NMDAR autoantibodies disrupt excitatory-inhibitory balance, leading to hippocampal network hypersynchrony

Graphical abstract

Authors

Mihai Ceanga, Vahid Rahmati,
Holger Haselmann, ..., Alessandro Ori,
Manfred Heckmann, Christian Geis

Correspondence

christian.geis@med.uni-jena.de

In brief

Ceanga et al. demonstrate hippocampal network dysfunction caused by patient-derived autoantibodies against the NMDA receptor. Using a passive-transfer mouse model, they uncover synaptic excitatory-inhibitory imbalance, ultimately triggering increased γ oscillations in brain slices, and identify a promising rescue strategy. These changes may underlie cognitive dysfunction and psychosis in autoimmune NMDA receptor encephalitis.

Highlights

- Human antibodies against the NMDAR cause hippocampal network dysfunction

- Reduced AMPAR signaling and faster synaptic inhibition lead to increased γ oscillations

- NMDAR antibodies induce corresponding changes in the hippocampal proteome

- Positive allosteric modulation of AMPARs rescues pathological network hypersynchrony

Cell Reports

Article

Human NMDAR autoantibodies disrupt excitatory-inhibitory balance, leading to hippocampal network hypersynchrony

Mihai Ceanga,[1,13] Vahid Rahmati,[1,13] Holger Haselmann,[1] Lars Schmidl,[1] Daniel Hunter,[2] Anna-Katherina Brauer,[3,4] Sabine Liebscher,[3,4,5] Jakob Kreye,[6,7,8] Harald Prüss,[6,7] Laurent Groc,[2] Stefan Hallermann,[9] Josep Dalmau,[10] Alessandro Ori,[11] Manfred Heckmann,[12] and Christian Geis[1,14,*]

[1]Section of Translational Neuroimmunology, Department of Neurology, Jena University Hospital, 07747 Jena, Germany
[2]Université de Bordeaux, CNRS, Interdisciplinary Institute for Neuroscience, UMR 5297, 33000 Bordeaux, France
[3]Institute of Clinical Neuroimmunology, Klinikum der Universität München, Ludwig Maximilians University Munich, Martinsried, Germany
[4]Biomedical Center, Ludwig Maximilians University Munich, Martinsried, Germany
[5]Munich Cluster for Systems Neurology (SyNergy), Munich, Germany
[6]Department of Neurology and Experimental Neurology, Charité – Universitätsmedizin Berlin, Corporate Member of Freie Universität Berlin and Humboldt-Universität zu Berlin, 10117 Berlin, Germany
[7]German Center for Neurodegenerative Diseases (DZNE) Berlin, Berlin, Germany
[8]Department of Pediatric Neurology, Charité – Universitätsmedizin Berlin, Corporate Member of Freie Universität Berlin and Humboldt-Universität zu Berlin, 10117 Berlin, Germany
[9]Carl Ludwig Institute for Physiology, Faculty of Medicine, Leipzig University, 04103 Leipzig, Germany
[10]Catalan Institution for Research and Advanced Studies (ICREA) and IDIBAPS-Hospital Clinic, University of Barcelona, 08036 Barcelona, Spain
[11]Leibniz Institute on Aging – Fritz Lipmann Institute (FLI), 07745 Jena, Germany
[12]Department of Neurophysiology, Institute of Physiology, University of Würzburg, 97070 Würzburg, Germany
[13]These authors contributed equally
[14]Lead contact
*Correspondence: christian.geis@med.uni-jena.de
https://doi.org/10.1016/j.celrep.2023.113166

SUMMARY

Anti-NMDA receptor autoantibodies (NMDAR-Abs) in patients with NMDAR encephalitis cause severe disease symptoms resembling psychosis and cause cognitive dysfunction. After passive transfer of patients' cerebrospinal fluid or human monoclonal anti-GluN1-autoantibodies in mice, we find a disrupted excitatory-inhibitory balance resulting from CA1 neuronal hypoexcitability, reduced AMPA receptor (AMPAR) signaling, and faster synaptic inhibition in acute hippocampal slices. Functional alterations are also reflected in widespread remodeling of the hippocampal proteome, including changes in glutamatergic and GABAergic neurotransmission. NMDAR-Abs amplify network γ oscillations and disrupt θ-γ coupling. A data-informed network model reveals that lower AMPAR strength and faster GABA$_A$ receptor current kinetics chiefly account for these abnormal oscillations. As predicted in silico and evidenced ex vivo, positive allosteric modulation of AMPARs alleviates aberrant γ activity, reinforcing the causative effects of the excitatory-inhibitory imbalance. Collectively, NMDAR-Ab-induced aberrant synaptic, cellular, and network dynamics provide conceptual insights into NMDAR-Ab-mediated pathomechanisms and reveal promising therapeutic targets that merit future in vivo validation.

INTRODUCTION

NMDA receptors (NMDARs) are ionotropic glutamate receptors that play a pivotal role in excitatory transmission and synaptic plasticity in the central nervous system (CNS). They are particularly important for memory formation and psychosocial behavior.[1] Hypofunction of NMDARs has been implicated in the pathophysiology of a variety of complex neuropsychiatric disorders; e.g., dementia or schizophrenia.[1,2] NMDAR encephalitis is a severe autoimmune CNS disorder whose symptoms are directly caused by highly specific pathogenic autoantibodies (Abs) that are produced by expanded B and plasma cells in the CNS, and target the amino-terminal domain of the GluN1 subunit of the NMDAR.[3,4]

NMDAR encephalitis is one of the most common subtypes of the newly described CNS disease group called autoimmune encephalitis,[5–7] with an incidence of about 1.2/100,000 person years, comparable with infectious encephalitides.[8] Affected patients suffer from a characteristic, severe and complex neuropsychiatric syndrome consisting of psychosis, memory
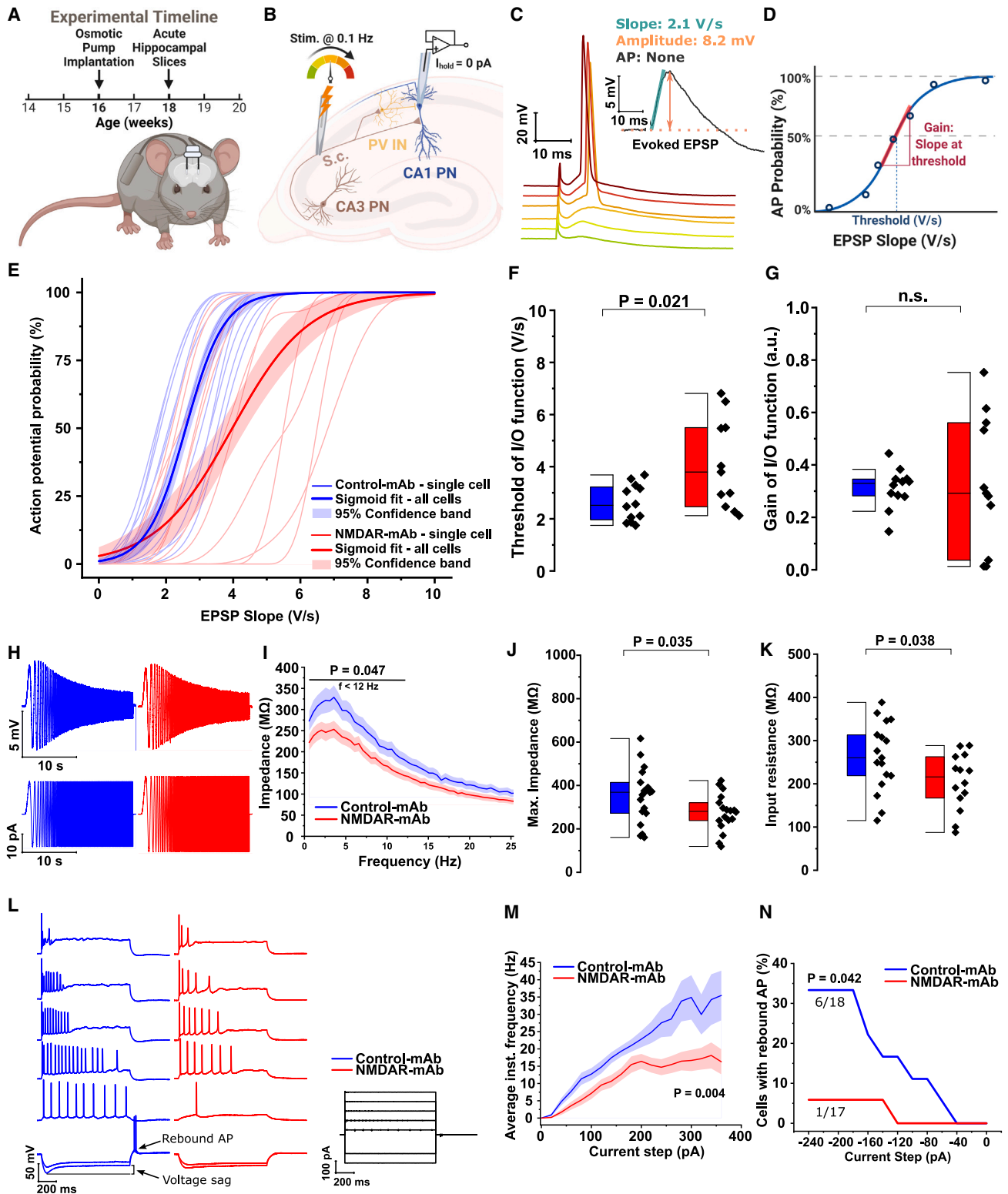
Figure 1. NMDAR-mAbs increase the I/O threshold and reduce intrinsic excitability in CA1 pyramidal neurons (PNs) *ex vivo*
(A and B) Schematic of the experimental timeline (A) and recording and stimulation configurations (B).
(C) Example response traces to incremental stimulation intensities, with the slope and amplitude of the resulting EPSP shown in the inset.

dysfunction, delusional thinking, hallucinations, catatonic features, epilepsy, and central hypoventilation.[4] Current standard treatment is based on immunotherapy,[9,10] which is often insufficient for symptom control in severely affected patients. Therefore, there is a medical need for a better understanding of antibody-induced network dysfunction and more specific treatment strategies.[11]

Binding of Abs to surface-expressed NMDARs induces cross-linking and internalization of these receptors, followed by a reduction in their surface expression in postsynaptic receptor fields, which reduces synaptic NMDAR currents and impairs long-term potentiation.[12–14] Passive transfer of NMDAR-Abs in animal models of the disease brought about cognitive and behavior disorders, reflecting a fundamental impairment of brain function. However, how the observed molecular changes affect computations at the single-cell and neural network levels remains largely unknown.

NMDAR hypofunction induced through genetic or pharmacological manipulation has been used previously to mimic symptoms of schizophrenia, which resembles key features in the clinical presentation of NMDAR encephalitis.[15,16] In these models, NMDAR hypofunction strongly disturbs synchronized neuronal activity patterns,[2,17,18] such as γ oscillations ($\sim$20–90 Hz).[19–21] These high-frequency oscillations provide a neural substrate of various cognitive processes, such as memory, learning, and spatial navigation.[22] To uncover the neural and network origins of the NMDAR-Ab-induced cognitive and behavioral abnormalities, we specifically investigated the effect of patient cerebrospinal fluid (CSF) or patient-derived monoclonal antibodies against the NMDAR-GluN1 subunit (NMDAR-mAbs) *ex vivo* in acute brain slices obtained from a passive-transfer mouse model mimicking antibody-induced disease signs of NMDAR encephalitis. We investigated network, intrinsic, and synaptic CA1 pyramidal neuron excitability, the hippocampal proteome, and hippocampal oscillations to gain in-depth insights into disease pathophysiology. These investigations identified neural and network impairments underlying NMDAR-Ab-induced brain dysfunction. Furthermore, they can propose specific therapeutic strategies aimed at rescuing these impairments. Last, they can offer insights into brain dysfunction in other pathologies linked to NMDAR hypofunction.

RESULTS

Synaptically driven CA1 neuronal output is reduced in acute brain slices of a passive-transfer mouse model of NMDAR-Ab encephalitis

NMDARs regulate neuronal excitability through synaptic plasticity mechanisms. Therefore, we hypothesized that Ab-induced NMDAR hypofunction would affect the neuronal input-output (I/O) function. We focused on CA1 pyramidal neurons (CA1-PNs) as the hippocampus read-outs. The I/O function of CA1 PNs is a fundamental computational property of the neuron and is mainly governed by the interplay between intrinsic excitability and synaptic inputs, driven largely by feedforward excitation (CA3→CA1) and inhibition (CA3→parvalbumin [PV]→CA1).[23,24] We used acute brain slices from an established passive-transfer mouse model with chronic intraventricular delivery of pathogenic immunoglobulin G (IgG).[14] We applied either NMDAR encephalitis patient-derived human monoclonal NMDAR-mAbs[25] and monoclonal control Abs (Control-mAbs as a reference) or direct patient-derived CSF containing high-titer NMDAR-Abs (NMDAR-CSF) and Control-CSF as a reference (Figure 1A). We then measured the synaptically driven I/O function of CA1 PNs after incremental stimulation of the Schaffer collaterals (SCs) in acute hippocampal slices (Figures 1B–1D). NMDAR-mAb treatment led to an increase in the I/O threshold (the excitatory postsynaptic potential [EPSP] slope with a 50% action potential [AP] generation probability) but did not change the I/O gain (the slope of the I/O curve at the threshold), although the variance of the gain was increased (Figures 1D–1G). Because changes in the excitatory-inhibitory (E-I) balance affect the gain and threshold of I/O function[23] as well as AP timing,[26,27] we next investigated subthreshold responses and AP properties of CA1 PNs. After NMDAR-mAb treatment, EPSP amplitudes were smaller for the same rise slope (Figure S1A) despite an unchanged membrane time constant (Figure S1G), suggesting alteration of the E-I balance. We observed loss of low-amplitude EPSPs, a deviation from the expected log-normal distribution,[28] and a marked reduction of EPSP peak latency dispersion in favor of shorter latencies (Figures S1B and S1D). Consequently, AP-eliciting EPSPs had higher slopes, while the AP latency distribution was narrower (Figure S1C). Feedforward inhibition and the E-I balance can also impact EPSP and spike timing.[29] We therefore analyzed EPSP

(D) The I/O function relates the binned EPSP slope to the AP probability per bin in the form of a sigmoid characterized by a threshold (EPSP slope with 50% AP probability) and gain (slope of the I/O curve at threshold).

(E) CA1 PN I/O function after NMDAR-mAb treatment. Curves are overall sigmoid fits ±95% confidence interval (CI). n = 12 cells/7 mice in Control-mAbs; n = 11 cells/5 mice in NMDAR-mAbs.

(F and G) The threshold (F) and gain (G) of the CA1 PN I/O function after NMDAR-mAb treatment. n as in (E).

(H) Example traces of the CA1 PN membrane impedance protocol.

(I) Impedance amplitude profile (ZAP) of CA1 PNs after NMDAR-mAb treatment. Curves are mean ± SEM. n = 19 cells/7 mice in Control-mAbs; n = 18 cells/6 mice in NMDAR-mAbs.

(J) Maximum impedance at resonant frequency decreases after NMDAR-mAb treatment. n as in (I).

(K) R_{in} decreases after NMDAR-mAb treatment. n = 17 cells/7 mice in Control-mAbs; n = 14 cells/6 mice in NMDAR-mAbs.

(L) Example traces during 1-s current injection at the soma (−250–360 pA in 20-pA steps).

(M) Average instantaneous firing frequency of CA1 PNs decreases after NMDAR-mAb treatment. Curves are mean ± SEM. n = 17 cells/7 mice in Control-mAbs; n = 17 cells/6 mice in NMDAR-mAbs.

(N) Rebound APs were nearly abolished by NMDAR-mAbs (at I_{cmd} = −240 pA). n = 18 cells/7 mice in Control-mAbs; n = 17 cells/6 mice in NMDAR-mAbs.

Boxplots represent median and interquartile range. Whiskers indicate outliers. Two-sample t test in (F), (G), (J), and (K). Two-tailed whole-curve permutation test in (M) and chi-square test in (N). See also Figure S1 and full statistical information in Table S1.

jitter and AP jitter and found both to be lower after NMDAR-mAb treatment (Figures S1E and S1F). Of note, the resting membrane potential (V_{rest}) and other AP properties, including the AP threshold, remained unchanged (Figures S1G and S1H). In conclusion, NMDAR-mAbs applied *in vivo* induces synaptic hypoexcitability of CA1 PNs *ex vivo* in acute brain slices, resulting in an increased I/O threshold as well as decreased EPSP and AP jitter.

Reduced AP firing after NMDAR-Ab treatment

Because plasticity of intrinsic excitability often co-occurs with synaptic plasticity,[24] we hypothesized that NMDAR-Abs alter CA1 PN intrinsic excitability. CA1 PNs show a prominent θ band (4–12 Hz) membrane resonance that promotes information transfer during subthreshold and network oscillations.[30] NMDAR-mAbs caused a reduction in impedance and input resistance (R_{in}) with no change in resonant frequency, V_{rest}, or membrane tau (Figures 1H–1K and S1G). Upon current-step injections, the mean instantaneous firing frequency was decreased by NMDAR-mAbs (Figures 1L and 1M), but there was no change in AP properties, the number of elicited Aps, or spike frequency adaptation (Figures S1H–S1K). CA1 PNs can also fire post-inhibitory rebound spikes. Upon membrane hyperpolarization, a lower proportion of PNs exhibited rebound APs after NMDAR-mAb treatment (Figure 1N) despite unchanged membrane voltage sag (Figure S1G). In sum, NMDAR-mAbs downregulate CA1 PN excitability by reducing membrane impedance and AP frequency and restricting rebound AP generation.

Reduced AMPA strength and faster GABA$_A$ kinetics in CA1 PNs after intraventricular infusion of NMDAR-Abs

An increased I/O threshold with unchanged gain suggests reduced synaptic excitation.[23] We therefore investigated the underlying synaptic currents by measuring spontaneous excitatory postsynaptic current (sEPSC; AMPA mediated) and spontaneous inhibitory postsynaptic current (sIPSC; GABA$_A$ mediated) inputs at the respective reversal potentials of inhibition and excitation (Figures 2 and S2A). NMDAR-mAbs reduced the amplitude, decay time constant (τ_d), and total charge transfer of sEPSC onto CA1 PNs in acute hippocampal slices but did not affect event frequency (Figures 2A–2G). Conversely, we observed no effect of NMDAR-mAbs on amplitude and frequency of sIPSC but a pronounced decrease in τ_d and charge transfer (Figures 2H–2N and S2B). Furthermore, sEPSC but not sIPSC event density was lower at the resonant frequency (Figures S2C and S2D), possibly contributing to the affected firing rate modulation by subthreshold resonance.[31] Moreover, using patient polyclonal NMDAR-CSF and Control-CSF, we similarly observed a reduced amplitude of AMPAR currents and a faster decay of GABA$_A$R currents (Figure S3). Next, we analyzed the dendritic and spine structure in CA1 PNs to investigate the structural basis of our observed changes in synaptic inputs. Reconstructing CA1 PNs in hippocampal sections revealed a negligible effect of NMDAR-mAbs on dendritic structures and spine distributions (Figure S4). Thus, functional rather than structural changes underlie the observed synaptic alterations. These data demonstrate decreased amplitude of AMPAR-mediated currents and faster decay kinetics of GABA$_A$R-mediated currents after NMDAR-Ab treatment.

NMDAR-Ab induces synaptic E-I imbalance and cell-specific changes in short-term plasticity

We next focused on coordinated evoked synaptic events of the CA3-to-CA1 feedforward microcircuit and measured the effect of NMDAR-Abs on the E-I balance in hippocampal slices *ex vivo*. We recorded CA1 PNs' compound postsynaptic currents at an intermediate holding potential (−35 mV; range, −40 to −25 mV) in response to single-pulse supramaximal SC stimulation. Evoked responses comprise an initial monosynaptic excitatory component (eESPC), followed by a delayed, balanced disynaptic inhibitory component (eIPSC) mediated largely by PV$^+$ interneurons (PV-INs),[32] which precisely controls gating and timing in the hippocampus[27] (Figures 3A and 3B). Corroborating our aforementioned results, NMDAR-mAbs increased the inhibitory-excitatory ratio (IER), indicating a shift toward stronger inhibition relative to excitation (Figures 3B and 3C). The integration window (the temporal distance between the peaks of evoked EPSC [eEPSC] and evoked IPSC [eIPSC]) was unchanged (Figure 3D). To disentangle the individual contributions of excitation and inhibition, we again stimulated SCs at the reversal potentials of inhibition (−70 mV) and excitation (−5 mV) and recorded monosynaptic eEPSC and disynaptic eIPSC, respectively. The I/O curve and maximal amplitudes of eEPSC were reduced after NMDAR-mAb treatment, with no evidence of a change in τ_d (Figures 3E–3H). We confirmed the unchanged amplitude (despite a higher variance) and faster decay kinetics of disynaptic eIPSC (Figures 3I–3L), as in our sIPSC data (Figures 2H–2N and S3B).

A recent study found changes in serial dependence, defined as a readout of passive information maintenance across trials, in patients with NMDAR encephalitis.[33] Computational modeling has linked serial dependence with short-term synaptic plasticity (STP).[34,35] Furthermore, STP can enhance spiking probability and reduce jitter in CA1 by modulating the IER.[36] We therefore evaluated the effect of NMDAR-Abs on STP. Under Control-mAbs, corroborating previous results,[36] the IER decreased and the integration time-window increased on the second pulse, promoting excitation and prolonging the integration time of excitatory inputs (Figures S5A–S5C). By contrast, under NMDAR-mAbs, the IER on the second pulse remained higher, and the integration window remained narrow, indicating less excitation during STP (Figures S5A–S5C). This can arise from decreased facilitation of CA3→CA1 PN synapses or attenuated depression at PV→CA1 PN synapses (further PV-IN recruitment through facilitation of CA3→PV is unlikely because stimulation was supramaximal). We therefore measured STP of eEPSC and found unchanged facilitation after NMDAR-mAb treatment (Figures S5D and S5E). Instead, we found pronounced NMDAR-mAb-induced attenuation of short-term depression in eIPSC (Figures S5F and S5G). Finally, we investigated whether excitatory input is affected upon high-frequency stimulation (100 pulses at 20 Hz; Figure S5H). Normalized eEPSC amplitudes decreased progressively and reached lower steady-state values under NMDAR-mAbs (Figures S5I–S5K), indicating persisting suppression of excitation during high-frequency stimulation.
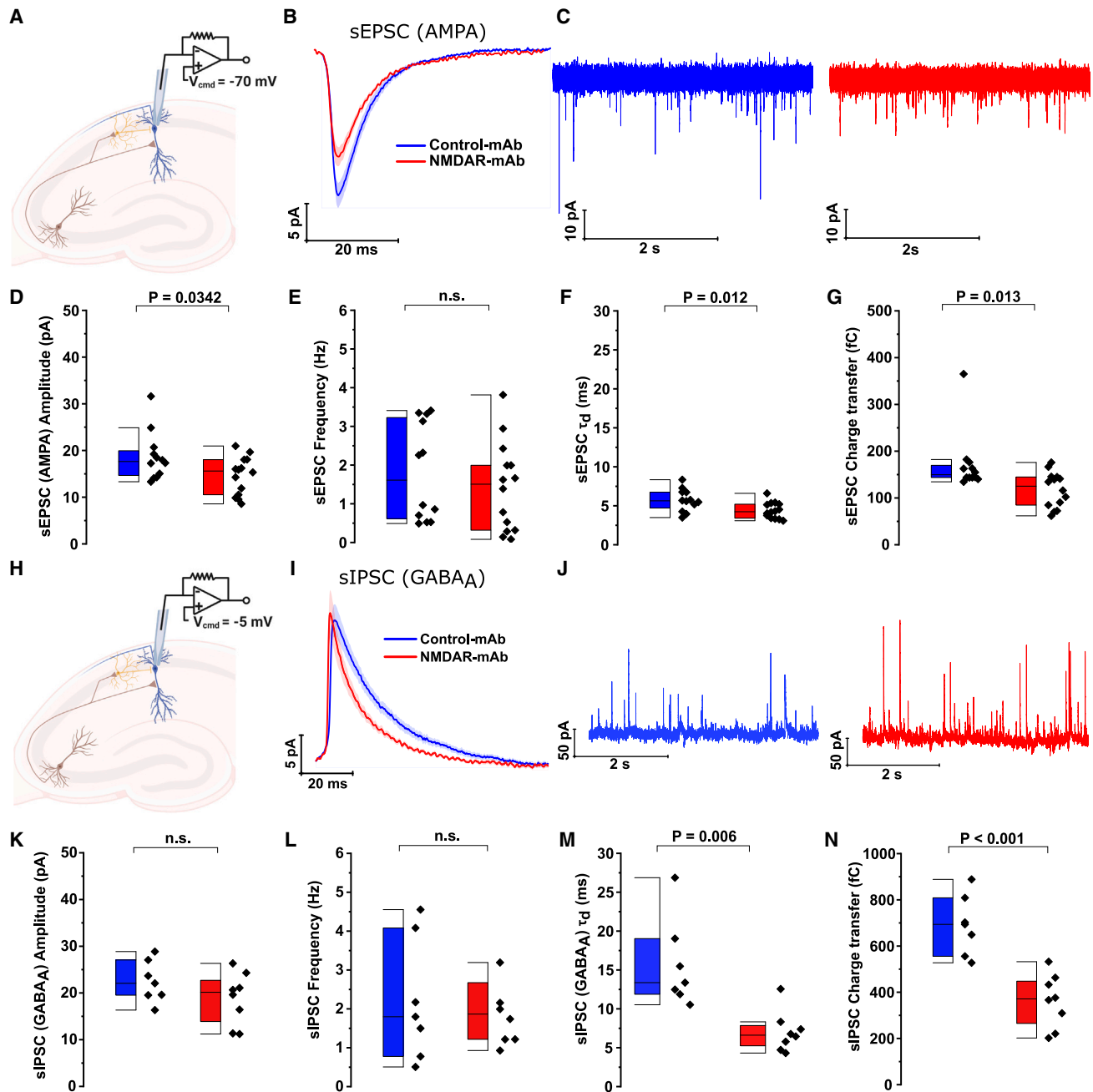
Figure 2. NMDAR-mAbs differentially affect AMPAR- and GABA$_A$R-mediated inputs onto CA1 PNs *ex vivo*

(A) Schematic of the recording configuration of sEPSC.

(B) Average sEPSC after NMDAR-mAb treatment. n = 12 cells/6 mice in Control-mAbs; n = 14 cells/6 mice in NMDAR-mAbs.

(C) Example traces of sEPSC.

(D–G) NMDAR-mAbs reduced the amplitude (D), decay time constant (F), and charge transfer (G) but not sEPSC frequency (E). n as in (B).

(H) Schematic of the recording configuration of sIPSC.

(I–N) Same as (B)–(G) but for sIPSC. NMDAR-mAbs reduce neither the amplitude (K) nor the frequency (L) of sIPSC but decrease the sIPSC decay time constant (M) and charge transfer of sIPSC (N). n = 7 cells/4 mice in Control-mAbs; n = 8 cells/4 mice in NMDAR-mAbs.

For (B) and (I), curves are mean ± SEM. Boxplots represent median and interquartile range. Whiskers indicate outliers. Mann-Whitney U test in (L), two-sample t tests in the rest. See also Figures S2, S3, and S4 and full statistical information in Table S1.
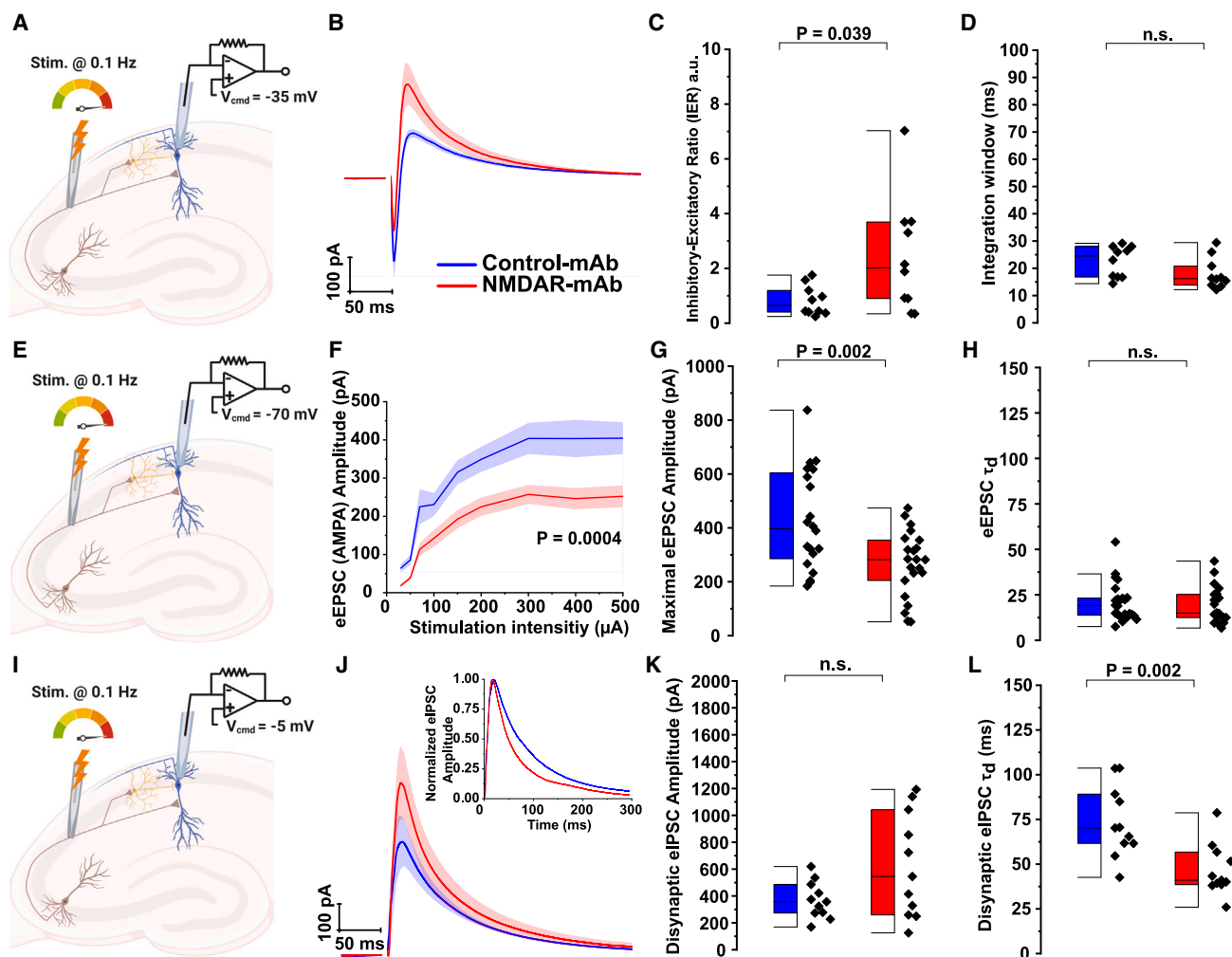
Figure 3. NMDAR-mAbs induce E-I imbalance in the CA3→CA1 feedforward circuit through reduced excitation *ex vivo*

(A) Schematic of the recording configuration of evoked biphasic postsynaptic response.

(B) Average biphasic response. n = 10 cells/4 mice in Control-mAbs; n = 10 cells/3 mice in NMDAR-mAbs.

(C) The inhibitory-excitatory ratio (IER) was increased after NMDAR-mAb treatment. n as in (B).

(D) The integration window remained unchanged. n as in (B).

(E) Schematic of the recording configuration of evoked EPSC (eEPSC).

(F) Reduced eEPSC amplitude after NMDAR-mAb treatment. n = 12 cells/6 mice in Control-mAbs; n = 14 cells/6 mice in NMDAR-mAbs.

(G and H) Reduced maximal eEPSC amplitude (G) but unchanged eEPSC decay time constant (H) after NMDAR-mAb treatment. n = 20 cells/6 mice in Control-mAbs; n = 22 cells/6 mice in NMDAR-mAbs.

(I) Schematic of the recording configuration of evoked disynaptic IPSC (eIPSC).

(J) Average eIPSC (inset: scaled) show the faster decay kinetics of eIPSC after NMDAR-mAb treatment. n = 11 cells/4 mice in Control-mAbs; n = 11 cells/3 mice in NMDAR-mAbs.

(K and L) Unchanged eIPSC amplitude (K) but reduced eIPSC decay time constant after NMDAR-mAb treatment. n as in (J).

For (B), (F), and (J), curves are mean ± SEM. Boxplots represent median and interquartile range. Whiskers indicate outliers. Two-sample t test in (F), (G), (J), and (K). Two-tailed whole-curve permutation test in (F), two-sample t tests in the rest. See also Figure S5 and full statistical information in Table S1.

In conclusion, NMDAR-Abs impair the hippocampal feedforward microcircuit by altering the synaptic E-I balance through reduced excitation and faster decay kinetics of inhibition.

Proteome remodeling reflects the functional changes induced by NMDAR-Abs

Because NMDAR-regulated synaptic plasticity often relies on protein synthesis, we next analyzed protein abundance changes in NMDAR-mAb-treated versus Control-mAb-treated hippocampi using data-independent acquisition mass spectrometry. We found significant abundance changes for 667 of 4,938 identified protein groups (Figure 4A; Table S2). To obtain mechanistic insight into affected pathways, we performed an over-representation analysis using Kyoto Encyclopedia of Genes and Genomes (KEGG) annotation. We observed significantly increased enrichment ratios in several key pathways involved in immune
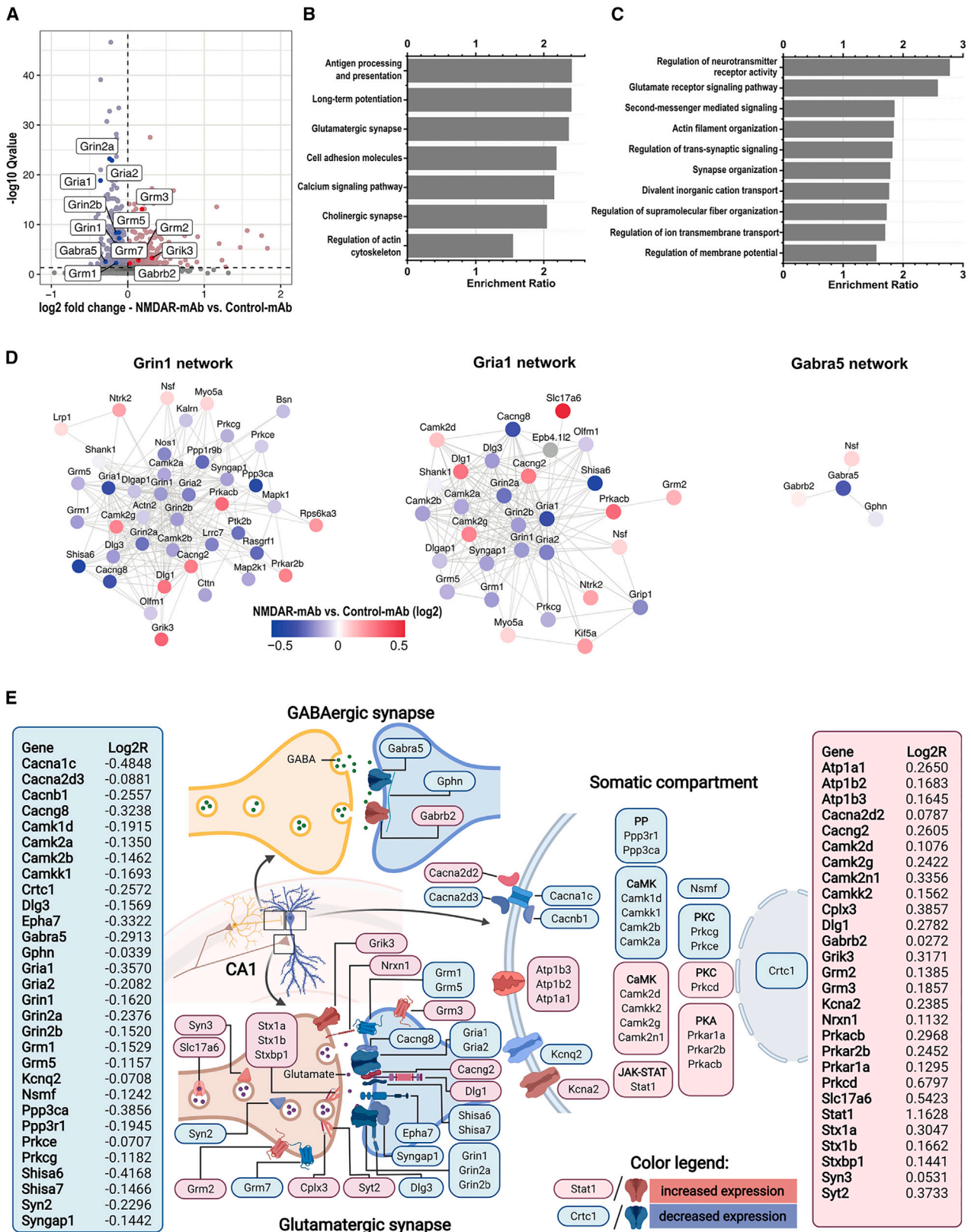
response (anting processing and presentation) and synaptic transmission (long-term potentiation, glutamatergic synapse; Figure 4B). We next conducted a Gene Ontology (GO) over-representation analysis that showed specific and significant regulation of pathways associated with synaptic transmission, second-messenger-mediated signaling, synapse organization, and membrane excitability, among others (Figure 4C). Accounting for the known functional effects of NMDAR-mAbs, the levels of Grin1, Grin2a, and Grin2b decreased (Figures 4D and 4E). However, the abundance of ionotropic and metabotropic glutamate receptors was also broadly affected, including AMPAR (Gria1 and Gria2), kainate receptors (KAR and Grik3), and group I (Grm1 and Grm5), II (Grm2 and Grm3), and III (Grm 7) metabotropic glutamate receptors (Figures 4A, 4D, and 4E; Table S2). In particular, our findings of reduced EPSC peak amplitudes and faster IPSC dynamics were reflected by a reduction of the protein levels of Gria1 and Gria2 as well as Gabra5, representing α5-subunit-containing GABA$_A$ receptors. These receptors are dendritically localized, show slow kinetics, and are preferentially activated by somatostatin INs[37] (Figures 4D and 4E). Overall, NMDAR-mAb-induced proteome remodeling affects several fundamental neuronal biochemical pathways and proteins, including NMDAR, AMPAR, and GABA$_A$R-α5-subunits. These abnormalities may account for molecular correlates of our observed electrophysiological changes.

Intraventricular NMDAR-Ab application leads to microglia activation

It has been questioned whether the passive-transfer model with chronic intraventricular infusion of NMDAR-Abs not only induces direct effects on the receptors but also leads to neuroinflammation, as seen in patients with NMDAR encephalitis.[6] In our KEGG enrichment analysis results, we also observed a significantly increased enrichment ratio in pathways associated with inflammation, such as systemic lupus erythematosus (enrichment ratio [ER] = 3.019), antigen processing and presentation (ER = 2.407), and Fc-γ receptor-mediated phagocytosis (ER = 1.7341). We next performed an immunohistochemical assessment of NMDAR-mAb-induced neuroinflammation by examining microglia morphology (Iba1 staining), activation (CD68 staining), and T cell infiltrates in the hippocampus (CD3 staining). We found an increased CD68$^+$/Iba1$^+$ ratio after NMDAR-mAb treatment, indicating an increase in activated microglia (Figures S6A and S6B). We did not identify T cell infiltration in the hippocampus, as would be expected after selective intraventricular IgG passive transfer. Detailed morphological analysis of microglia corroborated extensive microglia activation in mice after *in vivo*

NMDAR-mAb treatment. Microglia had significantly fewer segments per main branch, a shortened branch length, and a lower complexity of microglia processes reflected as reduced betweenness (Figures S6C–S6E). We also quantified the circularity of microglia, which assesses the compactness of the cells in 2D.[39] The circularity was increased after NMDAR-mAb treatment (Figure S6G), indicating a reduction of branch complexity in an activated state. Together, these morpho-functional signs indicate neuroinflammation with activated microglia in the presence of NMDAR-Abs, mirroring histopathological findings in patients with NMDAR encephalitis.

Abnormal amplification of γ oscillations by NMDAR-mAbs and NMDAR-CSF

Excitatory and inhibitory signaling onto PNs and INs (majorly the perisomatic-mediated inhibition by, e.g., PV-INs) determine γ oscillation (20–90 Hz) dynamics.[2,22,40,41] Because γ oscillations have key roles in various global and hippocampal functions, such as attentional selection, encoding, and retrieval of memory traces, among others,[22] we hypothesized that NMDAR-Abs alter γ oscillations in the hippocampal network.

To test this hypothesis, we used high-frequency stimulation (HFS) of SCs in acute hippocampal slices of mice treated with NMDAR-mAbs in comparison with Control-mAbs or with patient NMDAR-CSF in comparison with Control-CSF and recorded the extracellular local field potential (LFP) in the CA1 stratum pyramidale. HFS induced transient high-frequency oscillations in all groups (Figures 5A and S7B). These oscillations were stronger under NMDAR-mAbs and NMDAR-CSF (Figures 5B–5E and S7A–S7D) and mainly confined to the γ band (30–90 Hz) in all groups (Figures 5C, 5E, 5F, S7C, and S7E). In contrast to power strength, there was no change in their peak frequency and bandwidth (Figure 5F and S7E).

Furthermore, HFS also induced some concurrent θ oscillations (5–12 Hz) (Figures 5G and 5H). Hippocampal θ-nested γ oscillations are thought to represent a fundamental neural communication mechanism.[42,43] θ oscillations were seemingly disturbed and became less contingent with γ oscillations under NMDAR-mAbs (Figure 5G). This increase in γ oscillations and suppression of θ oscillations were even more pronounced under NMDAR-CSF compared with NMDAR-mAbs (Figures S7C–S7F). θ-γ co-modulation (TGC; the Pearson correlation between the amplitude envelope of each LFP signal in the θ and γ bands; STAR Methods) was reduced under NMDAR-mAbs, particularly between 100 and 350 ms (Figures 5H and 5I), which mainly relates to the period of significant increase in the power of γ oscillations (Figure 5E). Taken together, these *ex vivo* results indicate that

Figure 4. NMDAR-mAb-induced proteome changes

(A) Volcano plot of quantified proteins in hippocampi following NMDAR-mAb or Control-mAb treatment; n = 10 mice for each experimental group. Proteins that significantly (q < 0.05) increased or decreased in abundance following NMDAR-mAb treatment are highlighted in red and blue, respectively. Glutamate receptors affected by treatment with NMDAR-mAbs are annotated.

(B and C) Kyoto Encyclopedia of Genes and Genomes (KEGG) pathways (B) and GO biological processes (C) over-represented (false discovery rate [FDR] < 0.05) among proteins affected by NMDAR-mAb treatment.

(D) Network analysis centered on Grin1 (left), Gria1 (middle), and Gabra5 (right), showing interacting proteins affected by NMDAR-mAb treatment. Protein-protein interactions were retrieved from STRING[38] using a high confidence score ($\geq$0.7).

(E) Graphic representation of selected proteomic changes following NMDAR-mAb treatment.

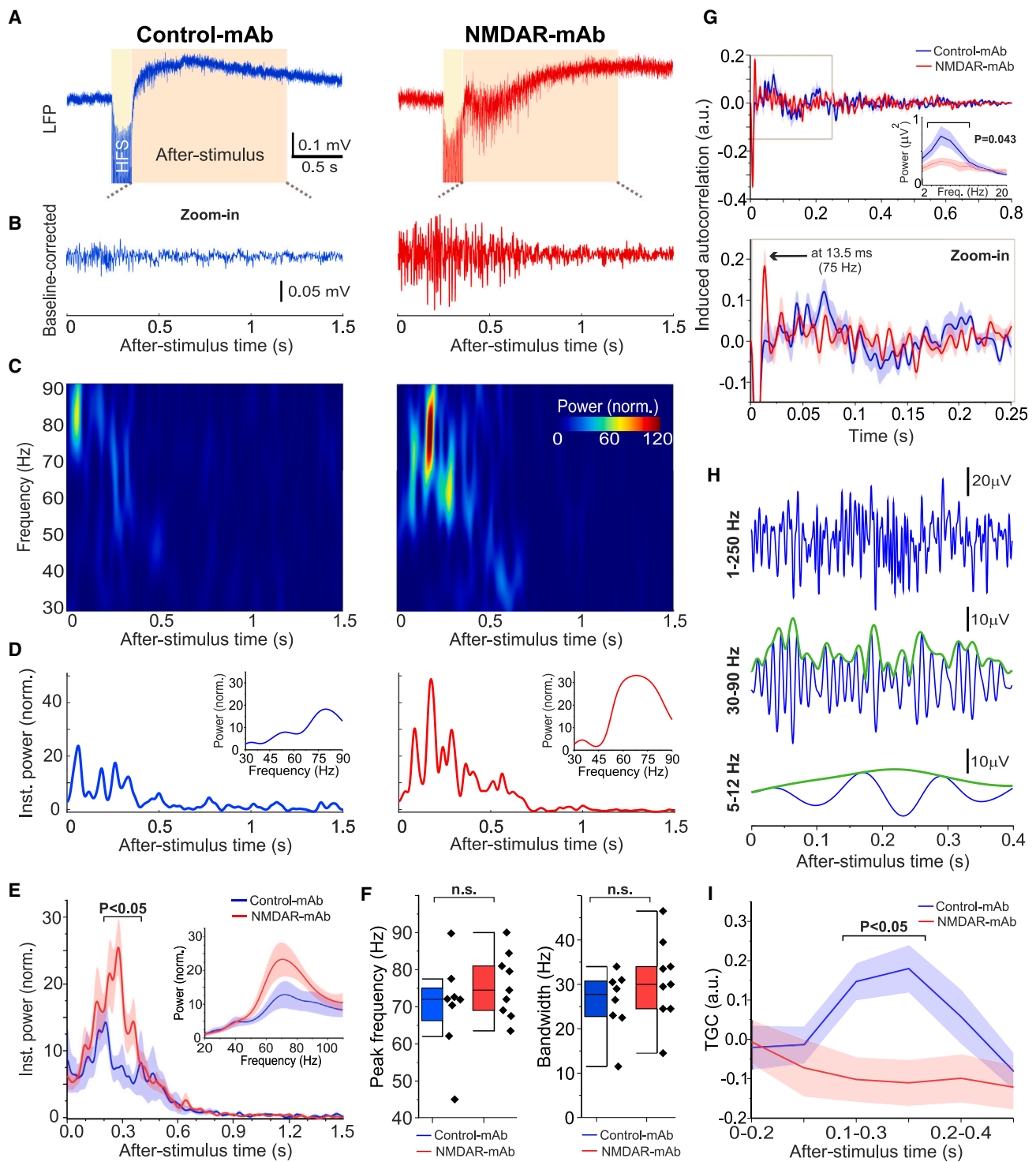See also Figure S6 and complete list of quantified proteins in Table S2.

Figure 5. NMDAR-mAbs amplify transiently induced γ oscillations in CA1 *ex vivo*

(A) Sample LFP traces of high-frequency stimulation (HFS) induced CA1 network oscillations in hippocampal slices. NMDAR-mAbs increase the amplitude of induced high-frequency oscillations.

(B) Magnification of 1.5 s of baseline-corrected LFPs (1.1–250 Hz) shown in (A).

(C) Time-frequency plots of LFPs shown in (B) for the γ band (30–90 Hz) and color-coded power of the after-HFS signal relative to the baseline.

(D) Same as (C) but for the total instantaneous γ-band power. Inset: wavelet-based power spectrum of HFS-induced γ oscillations.

anti-NMDAR Abs amplify the transiently induced γ oscillations and, at the same time, impair the CA1 information transfer mechanism of the θ-nested γ oscillations.

A CA1 neural network model identifies disinhibition of the PN-PV⁺ subnetwork as key to abnormal γ oscillation amplification

Our experimental data revealed amplification of γ oscillations because of NMDAR-Abs despite synaptic and intrinsic CA1 PN hypoexcitability. To gain mechanistic insights into this apparently paradoxical phenomenon, we combined our electrophysiological data with a well-established biophysical CA1 network model (Figure 6A) of θ-nested γ oscillations.[43–45] In brief, the model is composed of Hodgkin-Huxley-type neuron models of oriens lacunosum moleculare cells (O-LM or, briefly, O cells; inhibitory), pyramidal (E cells, excitatory), and fast-spiking PV⁺ cells (I cells, inhibitory). Following previous studies,[43,44] we modeled the E population as a single cell firing at the population frequency, thereby generating EPSPs in I cells (n = 10) and O cells (n = 10) at γ frequency, as observed experimentally.[46]

Figure 6A shows a typical simulated LFP (simLFP) signal in the Control model, emulating the reported θ-nested γ oscillations in CA1.[42,43] The spike rastergram shows that O cells fire preferentially and coherently at θ frequency and modulate the cycles of γ oscillations produced by the E-I subnetwork. We next investigated the key neural alterations underlying the aberrant γ oscillations by re-parameterizing the Control model. Our analysis revealed that implementing just two of the major changes seen in the NMDAR-Ab group can sufficiently account for the emerged aberrant oscillations (Figures 6B and 6D): the reduction in excitatory synaptic drive (e.g., through SCs) to E cells, $\varepsilon_{SC,E}$, reflecting reduced synaptic AMPAR signaling, and the reduced decay time constant of synaptic inhibitory projection of O cells, $\tau_{O,d}$, reflecting faster decay of GABA$_A$R currents. Under these two changes (NMDAR-Ab basal model), we found that γ-oscillatory power is strongly increased (Figures 6B and 6D), while its peak frequency is closely preserved (∼48–49 Hz). Moreover, O cells' firing coherence was largely lost at the population level, leading to a decrease in θ-oscillatory power (Figure 6B; see blue spike times). These results corroborate our experimental data (Figures 5 and S7). Importantly, inspection of spike rastergrams together with simLFP signals (Figure 6B) shows that O cells effectively fail in nesting the γ rhythm, thereby causing disinhibition of the E-I subnetwork, which, in turn, increases the amplitude and temporal continuity of γ oscillations. We further confirmed this finding by omitting the O population from the NMDAR-Ab basal model, where θ oscillations were largely abolished. Importantly, γ oscil-

lations underwent a similar amplification (compare models 1 and 2; Figures 6D and 6E). Mechanistically, these results suggest that disinhibition of the γ oscillation generator (E-I subnetwork), caused by O cell dysfunction, underlies the increased γ oscillations in the NMDAR-Ab group.

By applying the change in either $\varepsilon_{SC,E}$ or $\tau_{O,d}$ separately to the NMDAR-Ab basal model, we further found that neither of these changes individually (models 3 and 4; Figures 6D and 6E), but instead their combination (model 2), can reliably emulate our measured LFPs. Reducing R_{in} in E cells had a negligible effect (models 6 and 7 in Figures 6D and 6E). Moreover, reducing the decay time constant of fast inhibition mediated by I cells ($\tau_{I,d}$), instead of $\tau_{O,d}$, in the NMDAR-Ab basal model failed to reproduce our measured LFPs (model 5; Figures 6D and 6E). This implies that, from the overall reduction in τ_{decay} of the GABA$_A$ synapses onto CA1 PNs under NMDAR-Abs (Figures 2 and S3), including those from PV cells (Figures 3I–3L), the reduction in τ_{decay} of O-LM cells is the sufficient condition to account for the observed aberrant γ oscillations. In sum, these results suggest that the combined reductions in the time course of slow synaptic inhibition and the SC excitatory drive to E cells are the necessary and sufficient factors for γ oscillation amplification in the NMDAR-Ab group.

Theoretical studies predicted that faster inhibitory kinetics can counteract the disturbed network stability following NMDAR hypofunction.[47] Our modeling reaffirmed this by showing that the excessive θ- and γ-oscillatory activity emerging under NMDAR-Ab-induced reduction in ε_{SC} (model 3 in Figures 6D and 6E) can be suppressed by reductions in $\tau_{O,d}$ and $\tau_{I,d}$, respectively (Figure 6F; models 1 and 5 in Figures 6D and 6E). Moreover, we found that, whereas the sole reduction of $\varepsilon_{sc,c}$ lowered the γ peak frequency by ∼4 Hz (compare models 3 and 0 in Figure 6D), the reduction in IPSC time constant exerted an opposite effect by increasing this reduced frequency toward that in the Control model (Figure S8B). Of note, these effects of inhibitory synaptic time constant and the network input level on γ peak frequency are in accordance with previous modeling and experimental studies.[40,48] Altogether, corroborating theoretical predictions,[47] these results designate a compensatory role for the faster inhibitory kinetics observed after NMDAR-Ab treatment (Figures 2 and 3; see also discussion).

To investigate the significance of other plausible neural alterations under NMDAR-Abs, we extended our NMDAR-Ab basal model (Figure 6C). (1) We reduced the synaptic strength of all excitatory connections within CA1. (2) We reduced not only $\tau_{O,d}$ but also $\tau_{I,d}$ (Figures 2 and S3). (3) We reduced R_{in} of E cells (Figures 1I–1K). This extended model again exhibited an

(E) Average instantaneous HFS-induced γ-band power is increased after NMDAR-mAb treatment. Inset: average wavelet-based power spectrum of HFS-induced oscillations.

(F) Unchanged peak frequency and bandwidth (at half peak power) of γ oscillations after NMDAR-mAb treatment.

(G) θ oscillations are disrupted by NMDAR-mAbs. Top: autocorrelograms of the baseline-corrected LFPs after stimulus offset. Inset: multitaper power spectrum of the LFPs in the θ-band, showing a reduction in the induced θ-oscillatory power under NMDAR-mAbs. Bottom: magnification of the gray square in the top panel.

(H) Top: the first 400 ms of the Control-mAb LFP in (B). Middle: the same signal but band pass filtered in the γ band (blue), overlaid by its amplitude envelope (green). Bottom: same as middle but for the θ band.

(I) θ-γ Comodulation (TGC) is reduced by NMDAR-mAbs. TGC was computed for each window of size 0.2 s, with a sliding step of 0.050 s. n = 8 slices in Control-mAbs; n = 9 slices in NMDAR-mAbs.

In (E), (G), and (I), curves are mean ± SEM. Boxplots represent median and interquartile range. Whiskers indicate outliers. Two-sample t test in (F) and (G). Two-tailed permutation test of Cohen in (E) and (I). See also Figure S7 and full statistical information in Table S1.
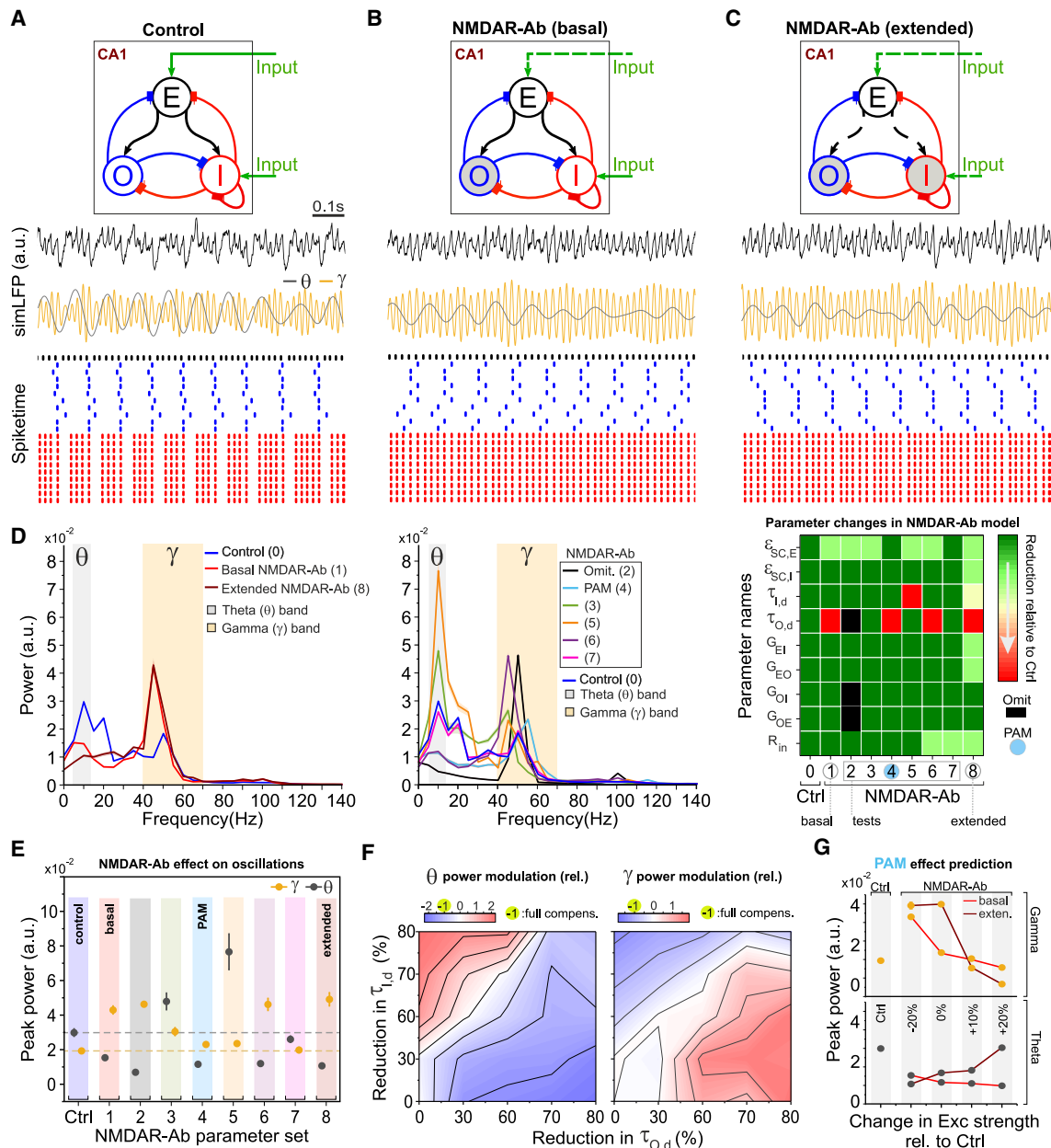
Figure 6. A CA1 network model identifies disinhibition of the PN-PV$^+$ subnetwork as underpinning γ amplification under NMDAR-Abs

(A) The model reproduces the hippocampal θ-nested γ oscillations using control parameterization. Top: schematic representing the synaptic connections among three distinct cell populations. E, pyramidal cells (excitatory); I, fast-spiking PV$^+$ cells (inhibitory); O, O-LM cells (inhibitory); input, excitatory synaptic drive to CA1, mediated by, e.g., Schaffer collaterals (SCs). Middle: example LFP signal simulated by the Control network model (simLFP), shown for 1 s (of 10 s). Bottom: corresponding band-pass-filtered simLFPs in θ and γ frequency bands. Bottom: corresponding spike rastergram of the model underlying the depicted simLFP.

(B) The dysfunction of O cells under NMDAR-Abs decreased θ oscillations and increased γ oscillations profoundly. Same as (A) but for the NMDAR-Ab basal model, which considers the reduction in SC excitatory drive to E cells $\varepsilon_{SC,E}$ (coded by a dashed line) and in the decay time constant of synaptic projection of O cells $\tau_{O,d}$ (coded by gray color).

(C) The main modeling results are robust against extrapolation of NMDAR-Ab effect on synaptic and membrane characteristics. Same as (B) but including a reduction in $\varepsilon_{SC,I}$, $\tau_{I,d}$, R_{in} of E cells, and synaptic weights of E to I and O populations (G_{EI} and G_{EO}). Similar results were obtained as in (B).

(D) Left: power spectrum of simLFPs shown in (A)–(C). Middle: same as left but for different parameterizations of the NMDAR-Ab model. Right: look-up map of parameter sets (1–8) of the changes used in the NMDAR-Ab model relative to the Control model (0). Exact values can be found in Table S3. Mean (solid line) ± SEM (shaded area).

(E) Peak power of θ oscillations and γ oscillations for the parameter sets shown in the look-up map in (D). Dots and whiskers are mean ± SEM.

(legend continued on next page)

increase in γ oscillations and suppression of θ oscillations (Figures 6C–6E). These results demonstrate the robustness of our modeling results and underscore the modulatory rather than essential role of these extensions in mediating γ oscillation amplification.

Finally, we found that removing the reduction of $\varepsilon_{SC,E}$ in the NMDAR-Ab basal model can effectively reinstate γ-oscillatory power (model 4; Figures 6D and 6E). As also confirmed in the NMDAR-Ab extended model, these results predict that sufficiently augmenting excitatory synaptic strength in the NMDAR-Ab group can markedly suppress the excessive γ oscillations (Figures 6G and S8A).

Application of the AMPA positive allosteric modulator (PAM) *ex vivo* alleviates abnormal γ oscillations

We next aimed to experimentally test not only our model predictions on modulation of AMPAR signaling (Figure 6G) but also whether γ oscillation amplification (Figures 5 and S7) is present in persistent network oscillations and in a pathway-independent manner (i.e., not only SCs). For this purpose, we chemically stimulated hippocampal slices using a bath application of 20 μM carbachol (CCH) and recorded LFP signals from the CA1 pyramidal layer.[49] Recordings were performed for 7 min to provide continuous rather than transient (Figure 5A) network oscillations, as in simLFP signals (Figures 6A–6C). CCH induced γ oscillations in both groups, again showing a profound increase in their power under NMDAR-mAbs, while preserving peak frequency at ∼25 Hz (Figures 7A and 7B). Moreover, by computing the time when the envelope autocorrelation of LFP signals drops below the 0.5 value (0.5 lag; Figures 7D and 7E),[50,51] we found an aberrant, higher autocorrelation of γ oscillations over longer time scales under NMDAR-Abs, as quantified by its higher 0.5 lag values (Figure 7D). This elevated autocorrelation under basal conditions may contribute to the reduced serial dependence in patients with NMDAR encephalitis[33] and the reduced accuracy during the early maintenance period of spatial working memory under NMDAR antagonists,[52] possibly through aberrant entangling of the memory traces of recently processed stimuli.

Finally, we experimentally tested our *in silico* model prediction about restoring the normal γ oscillations through augmenting the reduced excitatory synaptic strength (Figures 6G and S8A). We repeated the LFP recordings after bath application of CCH and a selective PAM of AMPARs (10 μM LY404187) to enhance AMPA signaling pharmacologically.[53] We found that the PAM, on average, suppresses γ oscillation peak power in the NMDAR-Ab group (note the dashed line at ∼0.1 μV² in Figures 7A and 7C), confirming our model prediction. Moreover, the PAM was able to restore the normal correlation level in the NMDAR-mAb group (Figure 7E) while not exerting a significant change in the Control-mAb group. Therefore, effective *ex vivo*

restoration of the normal γ oscillation characteristics by the AMPA PAM provides an opportunity for a target-directed rescue strategy in NMDAR-Ab encephalitis.

DISCUSSION

NMDARs are critical for brain function because of their important role in synaptic plasticity,[54] homeostatic scaling,[55] neuronal spike timing,[56] and persistent network activity.[57,58] Here, we provided in-depth insights into the open question of how long-term challenge of specific, patient-derived NMDAR mAbs and human CSF applied *in vivo* induce alterations of the hippocampal network as measured in acute hippocampal slice preparations *ex vivo*. These NMDAR-Ab-induced network abnormalities were validated using a computational model of hippocampal circuits. These changes may contribute to widespread, severe cognitive and behavioral deficits observed in patients with NMDAR encephalitis and in animal models with passive transfer of pathogenic Abs.[59–61] We specifically focused on potential impairment of E-I balance and network oscillations as important determinants of network and cognitive functions.[62,63] These same mechanisms are also altered in schizophrenia,[64,65] with which NMDAR encephalitis shares many similarities. Using proteomic, synaptic, cellular, and network-level measurements in the hippocampal CA1 *ex vivo*, we revealed a dual effect of pathogenic NMDAR-Abs. Whereas NMDAR-Abs induce synaptic and cellular hypoexcitability, they render network activity hypersynchronous in the γ band, with disrupted θ-γ coupling.

Using acute slices, we extensively investigated the hippocampal CA3→CA1 feedforward microcircuit, in which E-I balance dynamics directly gate and regulate the timing of PN activity.[26,27,29,66] NMDAR-Ab induced synaptic and intrinsic CA1 PN hypoexcitability and decreased AP jitter, which, in turn, may disturb the rate and spike-time coding.[67] Unchanged sIPSC amplitude and frequency together with unchanged disynaptic eIPSC amplitude suggest that the basal activity of, and fast excitatory drive onto, INs remain largely unaffected. Our findings regarding the changes in synaptic transmission in the hippocampus are in line with and extend the recent findings by Wright et al.[68] despite some methodological differences not allowing an exact comparison, such as measurements in different regions (CA1 vs. CA3). Furthermore, we found the STP of E-I balance to be perturbed by NMDAR-Abs, leading to a reduced excitatory integration window, which can limit coincidence detection[69] and the dynamic range for excitatory inputs onto CA1 PNs.[66,70] This STP perturbation may also account for the reduced serial dependence in patients with NMDAR encephalitis and schizophrenia[33] and should be tested in future *in vivo* experiments.

We also found a plethora of dysregulated proteins in the hippocampus after *in vivo* NMDAR-Ab treatment, which

(F) Compensatory role of faster inhibitory kinetics after NMDAR-Ab treatment. Shown are color-coded contour maps encoding the amount of change in the increased θ- (left) and γ-oscillatory powers (right) of model 3 in (D) through acceleration of synaptic inhibition. A value of −1 encodes full suppression of the excessive powers. The reductions (i.e., acceleration) of $\tau_{I,d}$ and $\tau_{O,d}$ are relative to the Control model.

(G) Augmenting Exc synaptic strength can reinstate γ- (top panel) and boost θ-oscillatory (bottom) powers. The changes in synaptic strength are relative to the Control model.
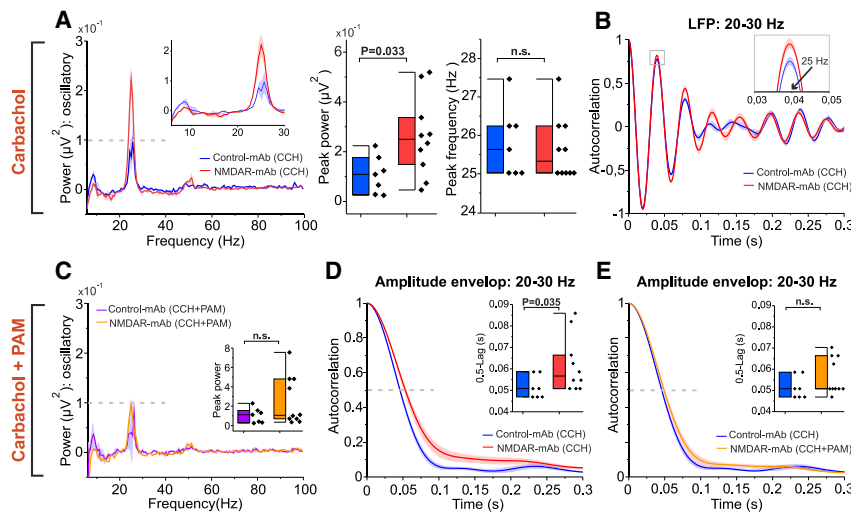
See also Figure S8, Table S3, and STAR Methods.

Figure 7. AMPA PAM suppresses NMDAR-mAb-induced amplification of persistent γ oscillations in CA1 *ex vivo*

(A) Left: power spectrum of carbachol (CCH) induced oscillations in CA1 *ex vivo*. Inset: magnification at lower frequency ranges. There is higher power of oscillations at ~20–30 Hz under NMDAR-mAbs compared with Control-mAbs and an opposite effect in the θ band (5–10 Hz). Median (solid line) ± jackknife standard error of median (shaded area). Middle: peak power of γ oscillations in the 20- 30-Hz band. Right: same as middle but for the peak frequency of γ oscillations. n = 7 slices in Control-mAbs; n = 10 slices in NMDAR-mAbs.

(B) Autocorrelograms of the LFPs band pass filtered between 20 and 30 Hz. Inset: magnification of the gray square.

(C) The AMPA PAM LY404187 (10 μM) tends to suppress excessive γ oscillation power caused by NMDAR-mAbs. Same as (A) but after additional application of the AMPA PAM. Inset: same as (A, middle) but under CCH+PAM application. n = 7 slices in Control-mAbs; n = 10 slices in NMDAR-mAbs.

(D) NMDAR-mAbs cause aberrant prolongation of the temporal correlation of γ oscillations. Autocorrelograms of the amplitude envelope of LFPs band pass filtered between 20 and 30 Hz. The dashed line designates the time when the autocorrelation drops below 0.5 value (0.5 lag time). Inset: boxplot of the 0.5 lag times.

(E) Same as (D) but for Control-mAbs (CCH) and NMDAR-mAbs (CCH+PAM).

Curves are mean ± SEM. Boxplots represent median and interquartile range. Whiskers indicate outliers. Two-sample t test in (A) (peak power), Mann-Whitney U test in (A) (peak frequency) and (C)–(E). See also Figure S7 and full statistical information in Table S1.

may be regarded as molecular correlates of the observed electrophysiological abnormalities. Virtually all major components of glutamatergic signaling were affected (AMPAR, NMDAR, KAR, and metabotropic receptor groups I, II, and III), as well as central hubs of intracellular signaling (including calcineurin [CaN], Ca^{2+}/calmodulin-dependent protein kinase [CaMK], protein kinase A [PKA], protein kinase C [PKC], and Stat1), raising the prospect of metaplasticity alterations. How NMDAR-Abs induce these changes, and whether they are primary or compensatory, remains to be determined. However, changes in AMPAR and KAR were also observed after chronic phencyclidine treatment,[71] indicating that NMDAR plays a primary role in resetting the strength of glutamatergic signaling. Changes in AMPAR (and AMPAR-associated proteins) may result from direct impairment of NMDAR-dependent homeostatic mechanisms of synaptic strength. Furthermore, several proteins that are strongly dysregulated in schizophrenia were also modified by NMDAR-Abs, highlighting possible common disease pathways (Cacna1c, Dlg1, Esyt1, Synpo, Dnm3, Shank,[72] etc.).

Identifying the specific neural alterations underpinning the abnormal γ amplification is important for understanding network dysfunction and developing treatment strategies. This is because γ oscillations have important roles in various interregional and hippocampal functions, such as learning, attentional selection, and working memory.[22] γ oscillations typically arise from the interaction between PNs and INs, whose synaptic current kinetics can modulate the power and frequency of these oscillations.[22,40,73] Accordingly, our findings of a reduced AMPAR-mediated drive and faster GABA$_A$R kinetics point to effective alteration of γ oscillations characteristics. Furthermore, our observed dominance of inhibition and the reduced EPSP and

AP jitter can also contribute to network hypersynchronicity.[74] By integrating our synaptic and cellular data into a biophysical CA1 network model, we found that neither of these changes individually, but instead their combination, can reliably emulate the oscillation characteristics in the NMDAR-Ab group. Of note, our recorded aberrant γ activity in hippocampal slices is in agreement with multiple studies based on genetic or pharmacologic manipulation of NMDAR, showing a robust alteration of γ oscillations because of NMDAR hypofunction (for a review, see Jadi et al.[2]).

The model predictions attribute pivotal importance to impaired INs projecting slow, rather than fast, GABAergic synapses (here, O-LM and PV cells, respectively). This, in turn, brings about disinhibition of the CA1 PN-PV γ generation subnetwork (the so-called pyramidal-interneuron γ [PING] network[44]), increasing γ-oscillatory power. Our modeling results suggest that this disinhibition is mainly due to failure of O-LM-cells to provide effective inhibition onto the PING network. This finding is supported by experimental evidence showing that inhibition arising from somatostatin⁺ INs (SOM-IN) onto PNs (and PVs) has a pivotal role in confining the excitatory net effect of SC (CA3→CA1), temporoammonic (EC→CA1), and hippocampal output pathways.[75–77] Remarkably, our model predicted that augmenting AMPAR signaling can restore the normal γ oscillations. Indeed, we showed that bath application of the AMPA PAM is able to effectively suppress excessive γ power in the NMDAR-Ab group, confirming this prediction experimentally.

O-LM cells also play a key role in generation of θ oscillations in the hippocampus.[46,78] Our *ex vivo* measurements and network modeling provide evidence of the alteration of these oscillations under NMDAR-Abs. Impaired θ oscillations were also found after NMDAR ablation in PV-INs[19] as well as a result

of disruption of O-LM cells[45] or through impaired inhibition onto PV-INs.[43]

It is still an open question what function these synaptic changes, resulting in aberrant γ oscillations, serve. This may be addressed by considering the experimentally supported role of relatively slow NMDAR-mediated currents in stabilizing global network activity and in emergence of stable (asynchronous) persistent working memory states.[47,57,58,79,80] Conceptually, NMDAR reduction can cause fast excitation to outpace reverberant inhibition, predisposing the network to instability (e.g., seizure-like activity) or hypersynchronous or self-driven oscillatory dynamics.[47,81] Similarly, impaired NMDAR-driven stability may explain data from CA3 after NMDAR-Ab treatment or region-specific deletion of NMDARs.[68,82] The ensuing aberrant oscillations can be detrimental to network stability, behavior, and function.[81,83]

Theoretical studies predicted two mechanisms amenable to compensate for the disturbed NMDAR-driven network stability; namely, weakening of AMPAR strength and acceleration of GABA$_A$R synaptic inhibition.[47,58] Whereas these predictions were mainly derived from cortical neural networks, our findings suggest a pathological role of reduced AMPAR strength in CA1. This is because our CA1 network model and *ex vivo* experimental data found AMPA PAM to normalize hippocampal rhythmogenesis in the NMDAR-Ab group. On the contrary, these data imply a homeostatic role of faster inhibition in a rhythm- and IN-type-selective manner: The NMDAR-Ab-affected CA1 network may prioritize alleviating the aberrant θ oscillations over γ oscillations by triggering a stronger homeostatic reduction in $\tau_{O,d}$ relative to $\tau_{I,d}$. Although this effectively suppresses excessive θ oscillations, it concurrently renders γ oscillations disinhibited. Nonetheless, the applicability of these findings, including the therapeutical effect of the AMPA PAM, requires future *in vivo* investigations. Collectively, the combination of our findings at proteomic, synaptic, single-neuron, and network levels provides insights into the antibody-induced pathophysiology of NMDAR encephalitis, which may guide future therapeutic opportunities. Moreover, it confirms that the complex disease pathophysiology in NMDAR encephalitis can indeed be developed on the basis of exclusive Ab-mediated NMDAR hypofunction without depending on additional concurrent Abs against other neuronal or currently unidentified targets.[25]

Patients with NMDAR encephalitis show intrathecal clonal expansion of self-directed B cells and long-lived plasma cells together with signs of neuroinflammation; e.g., microglia activation.[6,7] Different to other types of direct T cell-mediated encephalitis, cytotoxic T cell activation and neuronal destruction are much less evident.[6,7,84] Main disease symptoms therefore likely arise from Ab-induced alteration and (reversible) loss of NMDARs.[4,12,60,61] Here, by using a passive-transfer model of NMDAR-Abs, we aimed to uncover the effects of pathogenic Abs on the hippocampal network level; i.e., beyond solely on NMDAR malfunction. Evidently, the NMDAR-Ab passive-transfer model bypasses the initial steps of immune cell activation, in particular B cells and plasma cell expansion, but it shows key aspects of the disease pathophysiology, including direct NMDAR-Ab-induced pathophysiology and neuroinflammation. The mi-

croglia pathology is most likely driven by Fc-dependent immune activation induced by pathogenic tissue-bound NMDAR Abs. There are some active immunization models (e.g., immunization with NMDA holoreceptors or GluN1 ATD peptides), but they do not fully represent clinical and neuropathological characteristics as seen in patients with NMDAR encephalitis.[85,86] Therefore, the NMDAR-Ab passive-transfer model is so far the best-suited animal model to reproduce symptoms of disease that are specifically mediated by pathogenic Abs.

Our key findings were obtained by patient CSF and a specific, patient-derived mAb to NMDAR GluN1 with high affinity, which have been shown to induce the key pathogenic events in NDMAR encephalitis.[25,87,88] Furthermore, the similarities to schizophrenia at clinical and experimental levels and the mechanistic overlap of the disease pathophysiology reinforce the hypothesis that NMDAR hypofunction makes an important contribution to inducing characteristic disease symptoms in schizophrenia.

Limitations of the study

Although our adopted network model was sufficiently rich to reproduce and explain the changes in network oscillations, its identified mechanisms could prove more comprehensive by considering (1) the depressing STP of disynaptic inhibition onto CA1 PNs and (2) the important role of PVs, in addition to O-LM cells, in driving intrinsic CA1 θ oscillations.[89] Particularly, the key role of O-LM cells in the present model for driving θ and disinhibition of γ oscillations may be dependent on the connectivity regimens between O-LM and PV cells[90–92] and the pathway of the driving input or the θ-generator type.[89,93,94] Further detailed experimental studies on how different CA1 IN subclasses may be affected in the mouse model of NMDAR-Ab network dysfunction and incorporation in a computational neural network model may provide complementary insights into the role of INs and their plasticity in NMDAR-Ab-induced γ amplification.

A further limitation of the study includes analysis of only male mice, while a higher percentage of patients with NMDAR encephalitis is female. However, sex differences might be less relevant in the present work because here we address general principles of hippocampal network dysfunction rather than immunological mechanisms of Ab generation (e.g., triggered by ovarian teratomas).

Finally, although we provide in-depth mechanistic insights into potential disease-relevant hippocampal network dysfunction in *ex vivo* analyses of a validated passive-transfer model, future studies are required to assess their applicability to the *in vivo* situation with intact large-scale networks; e.g., including entorhinal inputs or medial septum rhythm generation. Therefore, our findings of NMDAR-Ab-induced γ oscillation amplification and its alleviation by the AMPA PAM need to be validated in *in vivo* models by combining behavioral analysis with continuous electrophysiological recordings of hippocampal oscillations.[19] This requires overcoming the technical challenges of implanting recording electrodes together with bilateral intraventricular catheters needed for the passive-transfer model. These technical limitations may become irrelevant when active immunization models showing reproducible disease symptoms based on

reliable production and CNS accessibility of disease-specific GluN1 antibodies are available.

STAR★METHODS

Detailed methods are provided in the online version of this paper and include the following:

- KEY RESOURCES TABLE
- RESOURCE AVAILABILITY
  - Lead contact
  - Materials availability
  - Data and code availability
- EXPERIMENTAL MODEL AND STUDY PARTICIPANT DETAILS
  - Animal model of NMDAR-encephalitis
  - Patient material
- METHOD DETAILS
  - Acute hippocampal preparation
  - Whole-cell recordings
  - Biocytin staining and morphologic analysis
  - Sample preparation for proteomics
  - Proteomics data acquisition
  - Proteomics data analysis
  - Histological analysis of mouse brain sections
  - Analysis of electrically induced oscillations
  - Analysis of chemically induced oscillations
  - Computational neural network model
  - Neuron models
  - Synaptic model
  - Model local field potential
  - Numeric and random aspects of model
  - Modulation of network oscillations
- QUANTIFICATION AND STATISTICAL ANALYSIS

SUPPLEMENTAL INFORMATION

Supplemental information can be found online at https://doi.org/10.1016/j.celrep.2023.113166.

INCLUSION AND DIVERSITY

We support inclusive, diverse, and equitable conduct of research.

REFERENCES

1. Paoletti, P., Bellone, C., and Zhou, Q. (2013). NMDA receptor subunit diversity: impact on receptor properties, synaptic plasticity and disease. Nat. Rev. Neurosci. *14*, 383–400. https://doi.org/10.1038/nrn3504.

2. Jadi, M.P., Behrens, M.M., and Sejnowski, T.J. (2016). Abnormal Gamma Oscillations in N-Methyl-D-Aspartate Receptor Hypofunction Models of Schizophrenia. Biol. Psychiatr. *79*, 716–726. https://doi.org/10.1016/j.biopsych.2015.07.005.

3. Dalmau, J., Tüzün, E., Wu, H.y., Masjuan, J., Rossi, J.E., Voloschin, A., Baehring, J.M., Shimazaki, H., Koide, R., King, D., et al. (2007). Paraneoplastic anti-N-methyl-D-aspartate receptor encephalitis associated with ovarian teratoma. Ann. Neurol. *61*, 25–36. https://doi.org/10.1002/ana.21050.

4. Dalmau, J., Geis, C., and Graus, F. (2017). Autoantibodies to Synaptic Receptors and Neuronal Cell Surface Proteins in Autoimmune Diseases of the Central Nervous System. Physiol. Rev. *97*, 839–887. https://doi.org/10.1152/physrev.00010.2016.

5. Dalmau, J., and Graus, F. (2018). Antibody-Mediated Encephalitis. N. Engl. J. Med. *378*, 840–851. https://doi.org/10.1056/NEJMra1708712.

6. Zrzavy, T., Endmayr, V., Bauer, J., Macher, S., Mossaheb, N., Schwaiger, C., Ricken, G., Winklehner, M., Glatter, S., Breu, M., et al. (2021). Neuropathological Variability within a Spectrum of NMDAR-Encephalitis. Ann. Neurol. *90*, 725–737. https://doi.org/10.1002/ana.26223.

7. Martinez-Hernandez, E., Horvath, J., Shiloh-Malawsky, Y., Sangha, N., Martinez-Lage, M., and Dalmau, J. (2011). Analysis of complement and plasma cells in the brain of patients with anti-NMDAR encephalitis. Neurology *77*, 589–593. https://doi.org/10.1212/WNL.0b013e318228c136.

8. Dubey, D., Pittock, S.J., Kelly, C.R., McKeon, A., Lopez-Chiriboga, A.S., Lennon, V.A., Gadoth, A., Smith, C.Y., Bryant, S.C., Klein, C.J., et al. (2018). Autoimmune encephalitis epidemiology and a comparison to infectious encephalitis. Ann. Neurol. *83*, 166–177. https://doi.org/10.1002/ana.25131.

9. Abboud, H., Probasco, J.C., Irani, S., Ances, B., Benavides, D.R., Bradshaw, M., Christo, P.P., Dale, R.C., Fernandez-Fournier, M., Flanagan, E.P., et al. (2021). Autoimmune encephalitis: proposed best practice recommendations for diagnosis and acute management. J. Neurol. Neurosurg. Psychiatry *92*, 757–768. https://doi.org/10.1136/jnnp-2020-325300.

10. Thaler, F.S., Zimmermann, L., Kammermeier, S., Strippel, C., Ringelstein, M., Kraft, A., Sühs, K.W., Wickel, J., Geis, C., Markewitz, R., et al. (2021). Rituximab Treatment and Long-term Outcome of Patients With Autoimmune Encephalitis: Real-world Evidence From the GENERATE Registry. Neurol. Neuroimmunol. Neuroinflamm. *8*, e1088. https://doi.org/10.1212/NXI.0000000000001088.

11. Sell, J., Haselmann, H., Hallermann, S., Hust, M., and Geis, C. (2021). Autoimmune encephalitis: novel therapeutic targets at the preclinical level. Expert Opin. Ther. Targets *25*, 37–47. https://doi.org/10.1080/14728222.2021.1856370.

12. Ladépêche, L., Planagumà, J., Thakur, S., Suárez, I., Hara, M., Borbely, J.S., Sandoval, A., Laparra-Cuervo, L., Dalmau, J., and Lakadamyali, M. (2018). NMDA Receptor Autoantibodies in Autoimmune Encephalitis Cause a Subunit-Specific Nanoscale Redistribution of NMDA Receptors. Cell Rep. *23*, 3759–3768. https://doi.org/10.1016/j.celrep.2018.05.096.

13. Hughes, E.G., Peng, X., Gleichman, A.J., Lai, M., Zhou, L., Tsou, R., Parsons, T.D., Lynch, D.R., Dalmau, J., and Balice-Gordon, R.J. (2010). Cellular and synaptic mechanisms of anti-NMDA receptor encephalitis. J. Neurosci. *30*, 5866–5875. https://doi.org/10.1523/JNEUROSCI.0167-10.2010.

14. Planagumà, J., Haselmann, H., Mannara, F., Petit-Pedrol, M., Grünewald, B., Aguilar, E., Röpke, L., Martín-García, E., Titulaer, M.J., Jercog, P., et al. (2016). Ephrin-B2 prevents N-methyl-D-aspartate receptor antibody effects on memory and neuroplasticity. Ann. Neurol. *80*, 388–400. https://doi.org/10.1002/ana.24721.

15. Maneta, E., and Garcia, G. (2014). Psychiatric manifestations of anti-NMDA receptor encephalitis: neurobiological underpinnings and differential diagnostic implications. Psychosomatics *55*, 37–44. https://doi.org/10.1016/j.psym.2013.06.002.

16. Kayser, M.S., and Dalmau, J. (2016). Anti-NMDA receptor encephalitis, autoimmunity, and psychosis. Schizophr. Res. *176*, 36–40. https://doi.org/10.1016/j.schres.2014.10.007.

17. Uhlhaas, P.J., and Singer, W. (2010). Abnormal neural oscillations and synchrony in schizophrenia. Nat. Rev. Neurosci. *11*, 100–113. https://doi.org/10.1038/nrn2774.

18. Fenton, A.A. (2015). Excitation-inhibition discoordination in rodent models of mental disorders. Biol. Psychiatr. *77*, 1079–1088. https://doi.org/10.1016/j.biopsych.2015.03.013.

19. Korotkova, T., Fuchs, E.C., Ponomarenko, A., von Engelhardt, J., and Monyer, H. (2010). NMDA receptor ablation on parvalbumin-positive interneurons impairs hippocampal synchrony, spatial representations, and working memory. Neuron *68*, 557–569. https://doi.org/10.1016/j.neuron.2010.09.017.

20. Tatard-Leitman, V.M., Jutzeler, C.R., Suh, J., Saunders, J.A., Billingslea, E.N., Morita, S., White, R., Featherstone, R.E., Ray, R., Ortinski, P.I., et al. (2015). Pyramidal cell selective ablation of NMDA-R1 causes increase in cellular and network excitability. Biol. Psychiatr. *77*, 556–568. https://doi.org/10.1016/j.biopsych.2014.06.026.

21. Billingslea, E.N., Tatard-Leitman, V.M., Anguiano, J., Jutzeler, C.R., Suh, J., Saunders, J.A., Morita, S., Featherstone, R.E., Ortinski, P.I., Gandal, M.J., et al. (2014). Parvalbumin cell ablation of NMDA-R1 causes increased resting network excitability with associated social and self-care deficits. Neuropsychopharmacology *39*, 1603–1613. https://doi.org/10.1038/npp.2014.7.

22. Buzsáki, G., and Wang, X.-J. (2012). Mechanisms of gamma oscillations. Annu. Rev. Neurosci. *35*, 203–225. https://doi.org/10.1146/annurev-neuro-062111-150444.

23. Carvalho, T.P., and Buonomano, D.V. (2009). Differential effects of excitatory and inhibitory plasticity on synaptically driven neuronal input-output functions. Neuron *61*, 774–785. https://doi.org/10.1016/j.neuron.2009.01.013.

24. Debanne, D., Inglebert, Y., and Russier, M. (2019). Plasticity of intrinsic neuronal excitability. Curr. Opin. Neurobiol. *54*, 73–82. https://doi.org/10.1016/j.conb.2018.09.001.

25. Kreye, J., Wenke, N.K., Chayka, M., Leubner, J., Murugan, R., Maier, N., Jurek, B., Ly, L.-T., Brandl, D., Rost, B.R., et al. (2016). Human cerebrospinal fluid monoclonal N-methyl-D-aspartate receptor autoantibodies are sufficient for encephalitis pathogenesis. Brain *139*, 2641–2652. https://doi.org/10.1093/brain/aww208.

26. Wahlstrom-Helgren, S., and Klyachko, V.A. (2016). Dynamic balance of excitation and inhibition rapidly modulates spike probability and precision in feed-forward hippocampal circuits. J. Neurophysiol. *116*, 2564–2575. https://doi.org/10.1152/jn.00413.2016.

27. Bhatia, A., Moza, S., and Bhalla, U.S. (2019). Precise excitation-inhibition balance controls gain and timing in the hippocampus. Elife *8*, e43415. https://doi.org/10.7554/eLife.43415.

28. Buzsáki, G., and Mizuseki, K. (2014). The log-dynamic brain: how skewed distributions affect network operations. Nat. Rev. Neurosci. *15*, 264–278. https://doi.org/10.1038/nrn3687.

29. Pouille, F., and Scanziani, M. (2001). Enforcement of temporal fidelity in pyramidal cells by somatic feed-forward inhibition. Science (New York, N.Y.) *293*, 1159–1163. https://doi.org/10.1126/science.1060342.

30. Hu, H., Vervaeke, K., Graham, L.J., and Storm, J.F. (2009). Complementary theta resonance filtering by two spatially segregated mechanisms in CA1 hippocampal pyramidal neurons. J. Neurosci. *29*, 14472–14483. https://doi.org/10.1523/JNEUROSCI.0187-09.2009.

31. Engel, T.A., Schimansky-Geier, L., Herz, A.V.M., Schreiber, S., and Erchova, I. (2008). Subthreshold membrane-potential resonances shape spike-train patterns in the entorhinal cortex. J. Neurophysiol. *100*, 1576–1589. https://doi.org/10.1152/jn.01282.2007.

32. Bartley, A.F., Lucas, E.K., Brady, L.J., Li, Q., Hablitz, J.J., Cowell, R.M., and Dobrunz, L.E. (2015). Interneuron Transcriptional Dysregulation Causes Frequency-Dependent Alterations in the Balance of Inhibition and Excitation in Hippocampus. J. Neurosci. *35*, 15276–15290. https://doi.org/10.1523/JNEUROSCI.1834-15.2015.

33. Stein, H., Barbosa, J., Rosa-Justicia, M., Prades, L., Morató, A., Galan-Gadea, A., Ariño, H., Martinez-Hernandez, E., Castro-Fornieles, J., Dalmau, J., and Compte, A. (2020). Reduced serial dependence suggests deficits in synaptic potentiation in anti-NMDAR encephalitis and schizophrenia. Nat. Commun. *11*, 4250. https://doi.org/10.1038/s41467-020-18033-3.

34. Kilpatrick, Z.P. (2018). Synaptic mechanisms of interference in working memory. Sci. Rep. *8*, 7879. https://doi.org/10.1038/s41598-018-25958-9.

35. Barbosa, J., Stein, H., Martinez, R.L., Galan-Gadea, A., Li, S., Dalmau, J., Adam, K.C.S., Valls-Solé, J., Constantinidis, C., and Compte, A. (2020). Interplay between persistent activity and activity-silent dynamics in the prefrontal cortex underlies serial biases in working memory. Nat. Neurosci. *23*, 1016–1024. https://doi.org/10.1038/s41593-020-0644-4.

36. Bartley, A.F., and Dobrunz, L.E. (2015). Short-term plasticity regulates the excitation/inhibition ratio and the temporal window for spike integration in CA1 pyramidal cells. Eur. J. Neurosci. *41*, 1402–1415. https://doi.org/10.1111/ejn.12898.

37. Schulz, J.M., Knoflach, F., Hernandez, M.-C., and Bischofberger, J. (2018). Dendrite-targeting interneurons control synaptic NMDA-receptor activation via nonlinear α5-GABAA receptors. Nat. Commun. *9*, 3576. https://doi.org/10.1038/s41467-018-06004-8.

38. Szklarczyk, D., Gable, A.L., Lyon, D., Junge, A., Wyder, S., Huerta-Cepas, J., Simonovic, M., Doncheva, N.T., Morris, J.H., Bork, P., et al. (2019). STRING v11: protein-protein association networks with increased coverage, supporting functional discovery in genome-wide experimental datasets. Nucleic Acids Res. *47*, D607–D613. https://doi.org/10.1093/nar/gky1131.

39. Heindl, S., Gesierich, B., Benakis, C., Llovera, G., Duering, M., and Liesz, A. (2018). Automated Morphological Analysis of Microglia After Stroke. Front. Cell. Neurosci. *12*, 106. https://doi.org/10.3389/fncel.2018.00106.

40. Brunel, N., and Wang, X.-J. (2003). What determines the frequency of fast network oscillations with irregular neural discharges? I. Synaptic dynamics and excitation-inhibition balance. J. Neurophysiol. *90*, 415–430. https://doi.org/10.1152/jn.01095.2002.

41. Nguyen, Q.-A., and Rubchinsky, L.L. (2021). Temporal patterns of synchrony in a pyramidal-interneuron gamma (PING) network. Chaos *31*, 043134. https://doi.org/10.1063/5.0042451.

42. Lisman, J.E., and Jensen, O. (2013). The θ-γ neural code. Neuron *77*, 1002–1016. https://doi.org/10.1016/j.neuron.2013.03.007.

43. Wulff, P., Ponomarenko, A.A., Bartos, M., Korotkova, T.M., Fuchs, E.C., Bähner, F., Both, M., Tort, A.B.L., Kopell, N.J., Wisden, W., and Monyer, H. (2009). Hippocampal theta rhythm and its coupling with gamma oscillations require fast inhibition onto parvalbumin-positive interneurons. Proc. Natl. Acad. Sci. USA *106*, 3561–3566. https://doi.org/10.1073/pnas.0813176106.

44. Cutsuridis, V., Graham, B., Cobb, S., and Vida, I. (2010). Hippocampal Microcircuits (Springer).

45. Duglad ze, T., Vida, I., Tort, A.B., Gross, A., Otahal, J., Heinemann, U., Kopell, N.J., and Gloveli, T. (2007). Impaired hippocampal rhythmogenesis in a mouse model of mesial temporal lobe epilepsy. Proc. Natl. Acad. Sci. USA *104*, 17530–17535. https://doi.org/10.1073/pnas.0708301104.

46. Gloveli, T., Dugladze, T., Saha, S., Monyer, H., Heinemann, U., Traub, R.D., Whittington, M.A., and Buhl, E.H. (2005). Differential involvement of oriens/pyramidale interneurones in hippocampal network oscillations in vitro. J. Physiol. *562*, 131–147. https://doi.org/10.1113/jphysiol.2004.073007.

47. Tegnér, J., Compte, A., and Wang, X.-J. (2002). The dynamical stability of reverberatory neural circuits. Biol. Cybern. *87*, 471–481. https://doi.org/10.1007/s00422-002-0363-9.

48. Lowet, E., De Weerd, P., Roberts, M.J., and Hadjipapas, A. (2022). Tuning Neural Synchronization: The Role of Variable Oscillation Frequencies in Neural Circuits. Front. Syst. Neurosci. *16*, 908665. https://doi.org/10.3389/fnsys.2022.908665.

49. Mann, E.O., Suckling, J.M., Hajos, N., Greenfield, S.A., and Paulsen, O. (2005). Perisomatic feedback inhibition underlies cholinergically induced fast network oscillations in the rat hippocampus in vitro. Neuron *45*, 105–117. https://doi.org/10.1016/j.neuron.2004.12.016.

50. Meisel, C., Bailey, K., Achermann, P., and Plenz, D. (2017). Decline of long-range temporal correlations in the human brain during sustained wakefulness. Sci. Rep. *7*, 11825. https://doi.org/10.1038/s41598-017-12140-w.

51. Honey, C.J., Thesen, T., Donner, T.H., Silbert, L.J., Carlson, C.E., Devinsky, O., Doyle, W.K., Rubin, N., Heeger, D.J., and Hasson, U. (2012). Slow cortical dynamics and the accumulation of information over long timescales. Neuron *76*, 423–434. https://doi.org/10.1016/j.neuron.2012.08.011.

52. Driesen, N.R., McCarthy, G., Bhagwagar, Z., Bloch, M.H., Calhoun, V.D., D'Souza, D.C., Gueorguieva, R., He, G., Leung, H.-C., Ramani, R., et al. (2013). The impact of NMDA receptor blockade on human working memory-related prefrontal function and connectivity. Neuropsychopharmacology *38*, 2613–2622. https://doi.org/10.1038/npp.2013.170.

53. Song, B., Lee, S., and Choi, S. (2012). LY404187, a potentiator of AMPARs, enhances both the amplitude and 1/CV2 of AMPA EPSCs but not NMDA EPSCs at CA3-CA1 synapses in the hippocampus of neonatal rats. Neurosci. Lett. *531*, 193–197. https://doi.org/10.1016/j.neulet.2012.10.020.

54. Lüscher, C., and Malenka, R.C. (2012). NMDA receptor-dependent long-term potentiation and long-term depression (LTP/LTD). Cold Spring Harbor Perspect. Biol. *4*, a005710. https://doi.org/10.1101/cshperspect.a005710.

55. Sutton, M.A., Ito, H.T., Cressy, P., Kempf, C., Woo, J.C., and Schuman, E.M. (2006). Miniature neurotransmission stabilizes synaptic function via tonic suppression of local dendritic protein synthesis. Cell *125*, 785–799. https://doi.org/10.1016/j.cell.2006.03.040.

56. Zick, J.L., Blackman, R.K., Crowe, D.A., Amirikian, B., DeNicola, A.L., Netoff, T.I., and Chafee, M.V. (2018). Blocking NMDAR Disrupts Spike Timing and Decouples Monkey Prefrontal Circuits: Implications for Activity-Dependent Disconnection in Schizophrenia. Neuron *98*, 1243–1255.e5. https://doi.org/10.1016/j.neuron.2018.05.010.

57. Wang, M., Yang, Y., Wang, C.-J., Gamo, N.J., Jin, L.E., Mazer, J.A., Morrison, J.H., Wang, X.-J., and Arnsten, A.F.T. (2013). NMDA Receptors Subserve Persistent Neuronal Firing During Working Memory In Dorsolateral Prefrontal Cortex. Neuron *77*, 736–749. https://doi.org/10.1016/j.neuron.2012.12.032.

58. Wang, X.J. (1999). Synaptic basis of cortical persistent activity: the importance of NMDA receptors to working memory. J. Neurosci. *19*, 9587–9603.

59. Heine, J., Kopp, U.A., Klag, J., Ploner, C.J., Prüss, H., and Finke, C. (2021). Long-Term Cognitive Outcome in Anti-N-Methyl-D-Aspartate Receptor Encephalitis. Ann. Neurol. *90*, 949–961. https://doi.org/10.1002/ana.26241.

60. Malviya, M., Barman, S., Golombeck, K.S., Planagumà, J., Mannara, F., Strutz-Seebohm, N., Wrzos, C., Demir, F., Baksmeier, C., Steckel, J., et al. (2017). NMDAR encephalitis: passive transfer from man to mouse by a recombinant antibody. Ann. Clin. Transl. Neurol. *4*, 768–783. https://doi.org/10.1002/acn3.444.

61. Planagumà, J., Leypoldt, F., Mannara, F., Gutiérrez-Cuesta, J., Martín-García, E., Aguilar, E., Titulaer, M.J., Petit-Pedrol, M., Jain, A., Balice-Gordon, R., et al. (2015). Human N-methyl D-aspartate receptor antibodies alter memory and behaviour in mice. Brain *138*, 94–109. https://doi.org/10.1093/brain/awu310.

62. van Vreeswijk, C., and Sompolinsky, H. (1996). Chaos in neuronal networks with balanced excitatory and inhibitory activity. Science (New York, N.Y.) *274*, 1724–1726. https://doi.org/10.1126/science.274.5293.1724.

63. Buzsáki, G. (2006). Rhythms of the Brain (Oxford University Press).

64. Uhlhaas, P.J., and Singer, W. (2015). Oscillations and neuronal dynamics in schizophrenia: the search for basic symptoms and translational opportunities. Biol. Psychiatr. *77*, 1001–1009. https://doi.org/10.1016/j.biopsych.2014.11.019.

65. Adams, R.A., Bush, D., Zheng, F., Meyer, S.S., Kaplan, R., Orfanos, S., Marques, T.R., Howes, O.D., and Burgess, N. (2020). Impaired theta phase coupling underlies frontotemporal dysconnectivity in schizophrenia. Brain *143*, 1261–1277. https://doi.org/10.1093/brain/awaa035.

66. Pouille, F., Marin-Burgin, A., Adesnik, H., Atallah, B.V., and Scanziani, M. (2009). Input normalization by global feedforward inhibition expands cortical dynamic range. Nat. Neurosci. *12*, 1577–1585. https://doi.org/10.1038/nn.2441.

67. Sjöström, P.J., Turrigiano, G.G., and Nelson, S.B. (2001). Rate, timing, and cooperativity jointly determine cortical synaptic plasticity. Neuron *32*, 1149–1164. https://doi.org/10.1016/s0896-6273(01)00542-6.

68. Wright, S.K., Rosch, R.E., Wilson, M.A., Upadhya, M.A., Dhangar, D.R., Clarke-Bland, C., Wahid, T.T., Barman, S., Goebels, N., Kreye, J., et al. (2021). Multimodal electrophysiological analyses reveal that reduced synaptic excitatory neurotransmission underlies seizures in a model of NMDAR antibody-mediated encephalitis. Commun. Biol. *4*, 1106. https://doi.org/10.1038/s42003-021-02635-8.

69. Fernández-Ruiz, A., Oliva, A., Soula, M., Rocha-Almeida, F., Nagy, G.A., Martin-Vazquez, G., and Buzsáki, G. (2021). Gamma rhythm communication between entorhinal cortex and dentate gyrus neuronal assemblies. Science *372*. https://doi.org/10.1126/science.abf3119.

70. Sylantyev, S., Savtchenko, L.P., O'Neill, N., and Rusakov, D.A. (2020). Extracellular GABA waves regulate coincidence detection in excitatory circuits. J. Physiol. *598*, 4047–4062. https://doi.org/10.1113/JP279744.

71. Barbon, A., Fumagalli, F., La Via, L., Caracciolo, L., Racagni, G., Riva, M.A., and Barlati, S. (2007). Chronic phencyclidine administration reduces the expression and editing of specific glutamate receptors in rat prefrontal cortex. Exp. Neurol. *208*, 54–62. https://doi.org/10.1016/j.expneurol.2007.07.009.

72. Föcking, M., Lopez, L.M., English, J.A., Dicker, P., Wolff, A., Brindley, E., Wynne, K., Cagney, G., and Cotter, D.R. (2015). Proteomic and genomic evidence implicates the postsynaptic density in schizophrenia. Mol. Psychiatr. *20*, 424–432. https://doi.org/10.1038/mp.2014.63.

73. Atallah, B.V., and Scanziani, M. (2009). Instantaneous modulation of gamma oscillation frequency by balancing excitation with inhibition. Neuron *62*, 566–577. https://doi.org/10.1016/j.neuron.2009.04.027.

74. Whittington, M.A., Traub, R.D., and Jefferys, J.G. (1995). Synchronized oscillations in interneuron networks driven by metabotropic glutamate receptor activation. Nature *373*, 612–615. https://doi.org/10.1038/373612a0.

75. Leão, R.N., Mikulovic, S., Leão, K.E., Munguba, H., Gezelius, H., Enjin, A., Patra, K., Eriksson, A., Loew, L.M., Tort, A.B.L., and Kullander, K. (2012). OLM interneurons differentially modulate CA3 and entorhinal inputs to hippocampal CA1 neurons. Nat. Neurosci. *15*, 1524–1530. https://doi.org/10.1038/nn.3235.

76. Haam, J., Zhou, J., Cui, G., and Yakel, J.L. (2018). Septal cholinergic neurons gate hippocampal output to entorhinal cortex via oriens lacunosum moleculare interneurons. Proc. Natl. Acad. Sci. USA *115*, E1886–E1895. https://doi.org/10.1073/pnas.1712538115.

77. Lovett-Barron, M., Turi, G.F., Kaifosh, P., Lee, P.H., Bolze, F., Sun, X.-H., Nicoud, J.-F., Zemelman, B.V., Sternson, S.M., and Losonczy, A. (2012). Regulation of neuronal input transformations by tunable dendritic inhibition. Nat. Neurosci. *15*, 423–430. https://doi.org/10.1038/nn.3024.

78. Buzsáki, G. (2002). Theta oscillations in the hippocampus. Neuron *33*, 325–340. https://doi.org/10.1016/s0896-6273(02)00586-x.

79. Compte, A., Brunel, N., Goldman-Rakic, P.S., and Wang, X.J. (2000). Synaptic mechanisms and network dynamics underlying spatial working memory in a cortical network model. Cerebr. Cortex *10*, 910–923. https://doi.org/10.1093/cercor/10.9.910.

80. Lisman, J.E., Fellous, J.M., and Wang, X.J. (1998). A role for NMDA-receptor channels in working memory. Nat. Neurosci. *1*, 273–275. https://doi.org/10.1038/1086.

81. Rahmati, V., Kirmse, K., Holthoff, K., Schwabe, L., and Kiebel, S.J. (2017). Developmental Emergence of Sparse Coding: A Dynamic Systems Approach. Sci. Rep. *7*, 13015. https://doi.org/10.1038/s41598-017-13468-z.

82. Fukushima, F., Nakao, K., Shinoe, T., Fukaya, M., Muramatsu, S.-I., Sakimura, K., Kataoka, H., Mori, H., Watanabe, M., Manabe, T., and Mishina, M. (2009). Ablation of NMDA receptors enhances the excitability of hippocampal CA3 neurons. PLoS One *4*, e3993. https://doi.org/10.1371/journal.pone.0003993.

83. Compte, A. (2006). Computational and in vitro studies of persistent activity: edging towards cellular and synaptic mechanisms of working memory. Neuroscience *139*, 135–151. https://doi.org/10.1016/j.neuroscience.2005.06.011.

84. Bauer, J., and Bien, C.G. (2016). Neuropathology of autoimmune encephalitides. Handb. Clin. Neurol. *133*, 107–120. https://doi.org/10.1016/B978-0-444-63432-0.00007-4.

85. Ding, Y., Zhou, Z., Chen, J., Peng, Y., Wang, H., Qiu, W., Xie, W., Zhang, J., and Wang, H. (2021). Anti-NMDAR encephalitis induced in mice by active immunization with a peptide from the amino-terminal domain of the GluN1 subunit. J. Neuroinflammation *18*, 53. https://doi.org/10.1186/s12974-021-02107-0.

86. Jones, B.E., Tovar, K.R., Goehring, A., Jalali-Yazdi, F., Okada, N.J., Gouaux, E., and Westbrook, G.L. (2019). Autoimmune receptor encephalitis in mice induced by active immunization with conformationally-sta-

87. bilized holoreceptors. Sci. Transl. Med. *11*, eaaw0044. https://doi.org/10.1126/scitranslmed.aaw0044.

87. Ly, L.-T., Kreye, J., Jurek, B., Leubner, J., Scheibe, F., Lemcke, J., Wenke, N.K., Reincke, S.M., and Prüss, H. (2018). Affinities of human NMDA receptor autoantibodies: implications for disease mechanisms and clinical diagnostics. J. Neurol. *265*, 2625–2632. https://doi.org/10.1007/s00415-018-9042-1.

88. Steinke, S., Kirmann, T., Loi, E.A., Nerlich, J., Weichard, I., Kuhn, P., Bullmann, T., Ritzau-Jost, A., Rizalar, F.S., Prüss, H., et al. (2023). NMDA-receptor-Fc-fusion constructs neutralize anti-NMDA receptor antibodies. Brain *146*, 1812–1820. https://doi.org/10.1093/brain/awac497.

89. Amilhon, B., Huh, C.Y.L., Manseau, F., Ducharme, G., Nichol, H., Adamantidis, A., and Williams, S. (2015). Parvalbumin Interneurons of Hippocampus Tune Population Activity at Theta Frequency. Neuron *86*, 1277–1289. https://doi.org/10.1016/j.neuron.2015.05.027.

90. Ferguson, K.A., Huh, C.Y.L., Amilhon, B., Manseau, F., Williams, S., and Skinner, F.K. (2015). Network models provide insights into how oriens-lacunosum-moleculare and bistratified cell interactions influence the power of local hippocampal CA1 theta oscillations. Front. Syst. Neurosci. *9*, 110. https://doi.org/10.3389/fnsys.2015.00110.

91. Müller, C., and Remy, S. (2014). Dendritic inhibition mediated by O-LM and bistratified interneurons in the hippocampus. Front. Synaptic Neurosci. *6*, 23. https://doi.org/10.3389/fnsyn.2014.00023.

92. Antonoudiou, P., Tan, Y.L., Kontou, G., Upton, A.L., and Mann, E.O. (2020). Parvalbumin and Somatostatin Interneurons Contribute to the Generation of Hippocampal Gamma Oscillations. J. Neurosci. *40*, 7668–7687. https://doi.org/10.1523/JNEUROSCI.0261-20.2020.

93. López-Madrona, V.J., Pérez-Montoyo, E., Álvarez-Salvado, E., Moratal, D., Herreras, O., Pereda, E., Mirasso, C.R., and Canals, S. (2020). Different theta frameworks coexist in the rat hippocampus and are coordinated during memory-guided and novelty tasks. Elife *9*, e57313. https://doi.org/10.7554/eLife.57313.

94. Huh, C.Y.L., Amilhon, B., Ferguson, K.A., Manseau, F., Torres-Platas, S.G., Peach, J.P., Scodras, S., Mechawar, N., Skinner, F.K., and Williams, S. (2016). Excitatory Inputs Determine Phase-Locking Strength and Spike-Timing of CA1 Stratum Oriens/Alveus Parvalbumin and Somatostatin Interneurons during Intrinsically Generated Hippocampal Theta Rhythm. J. Neurosci. *36*, 6605–6622. https://doi.org/10.1523/JNEUROSCI.3951-13.2016.

95. Perez-Riverol, Y., Csordas, A., Bai, J., Bernal-Llinares, M., Hewapathirana, S., Kundu, D.J., Inuganti, A., Griss, J., Mayer, G., Eisenacher, M., et al. (2019). The PRIDE database and related tools and resources in 2019: improving support for quantification data. Nucleic Acids Res. *47*, D442–D450. https://doi.org/10.1093/nar/gky1106.

98. Kilkenny, C., Browne, W.J., Cuthill, I.C., Emerson, M., and Altman, D.G. (2010). Improving bioscience research reporting: the ARRIVE guidelines for reporting animal research. PLoS Biol. *8*, e1000412. https://doi.org/10.1371/journal.pbio.1000412.

99. Petit-Pedrol, M., Sell, J., Planagumà, J., Mannara, F., Radosevic, M., Haselmann, H., Ceanga, M., Sabater, L., Spatola, M., Soto, D., et al. (2018). LGI1 antibodies alter Kv1.1 and AMPA receptors changing synaptic excitability, plasticity and memory. Brain *141*, 3144–3159. https://doi.org/10.1093/brain/awy253.

100. Ceanga, M., Keiner, S., Grünewald, B., Haselmann, H., Frahm, C., Couillard-Després, S., Witte, O.W., Redecker, C., Geis, C., and Kunze, A. (2019). Stroke Accelerates and Uncouples Intrinsic and Synaptic Excitability Maturation of Mouse Hippocampal DCX+ Adult-Born Granule Cells. J. Neurosci. *39*, 1755–1766. https://doi.org/10.1523/JNEUROSCI.3303-17.2018.

101. Dewell, R.B., and Gabbiani, F. (2019). Active membrane conductances and morphology of a collision detection neuron broaden its impedance profile and improve discrimination of input synchrony. J. Neurophysiol. *122*, 691–706. https://doi.org/10.1152/jn.00048.2019.

102. Tohidi, V., and Nadim, F. (2009). Membrane resonance in bursting pacemaker neurons of an oscillatory network is correlated with network frequency. J. Neurosci. *29*, 6427–6435. https://doi.org/10.1523/JNEUROSCI.0545-09.2009.

103. Gloveli, T., Dugladze, T., Rotstein, H.G., Traub, R.D., Monyer, H., Heinemann, U., Whittington, M.A., and Kopell, N.J. (2005). Orthogonal arrangement of rhythm-generating microcircuits in the hippocampus. Proc. Natl. Acad. Sci. USA *102*, 13295–13300. https://doi.org/10.1073/pnas.0506259102.

104. Buczak, K., Kirkpatrick, J.M., Truckenmueller, F., Santinha, D., Ferreira, L., Roessler, S., Singer, S., Beck, M., and Ori, A. (2020). Spatially resolved analysis of FFPE tissue proteomes by quantitative mass spectrometry. Nat. Protoc. *15*, 2956–2979. https://doi.org/10.1038/s41596-020-0356-y.

105. Storey, J.D. (2002). A direct approach to false discovery rates. J. Roy. Stat. Soc. B *64*, 479–498. https://doi.org/10.1111/1467-9868.00346.

106. Liao, Y., Wang, J., Jaehnig, E.J., Shi, Z., and Zhang, B. (2019). WebGestalt 2019: gene set analysis toolkit with revamped UIs and APIs. Nucleic Acids Res. *47*, W199–W205. https://doi.org/10.1093/nar/gkz401.

107. Cohen, M.X. (2014). Analyzing Neural Time Series Data: Theory and Practice (The MIT Press).

96. Mitra, P. (2008). Observed Brain Dynamics (Oxford University Press USA - OSO).

108. Shirvalkar, P.R., Rapp, P.R., and Shapiro, M.L. (2010). Bidirectional changes to hippocampal theta-gamma comodulation predict memory for recent spatial episodes. Proc. Natl. Acad. Sci. USA *107*, 7054–7059. https://doi.org/10.1073/pnas.0911184107.

97. Wen, H., and Liu, Z. (2016). Separating Fractal and Oscillatory Components in the Power Spectrum of Neurophysiological Signal. Brain Topogr. *29*, 13–26. https://doi.org/10.1007/s10548-015-0448-0.

109. Tort, A.B.L., Rotstein, H.G., Dugladze, T., Gloveli, T., and Kopell, N.J. (2007). On the formation of gamma-coherent cell assemblies by oriens lacunosum-moleculare interneurons in the hippocampus. Proc. Natl. Acad. Sci. USA *104*, 13490–13495. https://doi.org/10.1073/pnas.0705708104.

110. Tsodyks, M.V., Skaggs, W.E., Sejnowski, T.J., and McNaughton, B.L. (1997). Paradoxical effects of external modulation of inhibitory interneurons. J. Neurosci. *17*, 4382–4388.

111. Flossmann, T., Kaas, T., Rahmati, V., Kiebel, S.J., Witte, O.W., Holthoff, K., and Kirmse, K. (2019). Somatostatin Interneurons Promote Neuronal Synchrony in the Neonatal Hippocampus. Cell Rep. *26*, 3173–3182.e5. https://doi.org/10.1016/j.celrep.2019.02.061.

112. Olufsen, M.S., Whittington, M.A., Camperi, M., and Kopell, N. (2003). New roles for the gamma rhythm: population tuning and preprocessing for the Beta rhythm. J. Comput. Neurosci. *14*, 33–54. https://doi.org/10.1023/A:1021124317706.

113. Ermentrout, G.B., and Kopell, N. (1998). Fine structure of neural spiking and synchronization in the presence of conduction delays. Proc. Natl. Acad. Sci. USA *95*, 1259–1264. https://doi.org/10.1073/pnas.95.3.1259.

114. Wang, X.-J., and Buzsáki, G. (1996). Gamma Oscillation by Synaptic Inhibition in a Hippocampal Interneuronal Network Model. J. Neurosci. *16*, 6402–6413. https://doi.org/10.1523/JNEUROSCI.16-20-06402.1996.

115. Saraga, F., Wu, C.P., Zhang, L., and Skinner, F.K. (2003). Active dendrites and spike propagation in multi-compartment models of oriens-lacunosum/moleculare hippocampal interneurons. J. Physiol. *552*, 673–689. https://doi.org/10.1113/jphysiol.2003.046177.

116. Carnevale, N.T., and Hines, M.L. (2006). The NEURON Book (Cambridge University Press).

STAR★METHODS

KEY RESOURCES TABLE

REAGENT or RESOURCE	SOURCE	IDENTIFIER
Antibodies		
goat anti human Cy3	Dianova	109-165-003; RRID: AB_3065049
anti-Iba-1	Wako	#019-19741; RRID:AB_839504
goat anti rabbit AF 647	Invitrogen	A32733; RRID:AB_2633282
mouse anti-Cy3	abcam	Cat# ab52060; RRID:AB_873746
anti-CD68 antibody	Bio-Rad	#MCA1957; RRID:AB_322219
donkey anti rat AF 647	Jackson ImmunoResearch	#712-606-150; RRID: AB_2340695
anti-CD3 antibody	BioLegend	#100201; RRID: AB_312658
goat anti rat	Invitrogen	#A11006; RRID: AB_2534074
Biological samples		
Human monoclonal NMDAR-antibody	H. Prüss lab[25]	#003-102
Human monoclonal control-antibody	H. Prüss lab[25]	#mGO53
NMDAR-encephalitis patient-derived CSF	This data	N/A
Control patient-derived CSF	This data	N/A
Chemicals, peptides, and recombinant proteins		
N-Methyl-D-Glucamine	Sigma-Aldrich	M2004-500G
$NaHCO_3$	Roth	HN01.1
NaCl	Roth	HN00.2
KCl	Merck	1.04936.0500
NaH_2PO_4	Roth	2370.1
$MgSO_4$	Roth	0682.3
$MgCl_2$	Roth	2189.2
$CaCl_2$	Roth	HN04.3
HEPES	Roth	HN77.3
Glucose	Roth	HN06.3
Thiourea	Sigma	T8656-100G
Na-ascorbate	Sigma-Aldrich	11140-50G
Na-pyruvate	Sigma-Aldrich	P8574-25G
N-acetylcysteine	Sigma-Aldrich	A7250-100G
$CsMeSO_4$	Sigma	C1426-25G
CsCl	Sigma-Aldrich	203025-10G
EGTA	Sigma	E3889-25G
Spermine	Fluka	85590-5G
QX-314-Br	Tocris	1014
Mg_2-ATP	Sigma	A9187-500MG
Na_2-GTP	Sigma	G8877-250MG
Phosphocreatine	Sigma	P7936-5G
K-Gluconate	Sigma	G4500-100
Biocytin	Tocris	3349-50mg
AM-251	Tocris	1117
Carbachol	Sigma	C4382-1G
LY404187	Tocris	5297
Triton X-100	Sigma-Aldrich	93443-100ML
Entellan	Merck	1079610100

Continued

REAGENT or RESOURCE	SOURCE	IDENTIFIER
AP-5	Tocris	0106
Streptavidin-Cy3	Sigma	S6402-1ML
Lipofectamine™ 3000 Transfection Reagent	ThermoFisher Scientific	L3000008
Deposited data		
Mass spectrometry proteomics	This data	ProteomeXchange: PXD032055; username: reviewer_pxd032055@ebi.ac.uk password: kPyDcasn
Experimental models: Cell lines		
Primary hippocampal neuronal cultures	This data	N/A
HEK293 cultures	This data	N/A
Experimental models: Organisms/strains		
C57BL/6J	Local animal facility	N/A
Recombinant DNA		
GluN1-eGFP plasmid	Technicion Faculty of Medicine, Haifa	NR1a:GFP pEGFP-N3 NR1: NM_017010.2
GluN2A plasmid	MPI MF Heidelberg	NR2A pRK7 NR2A: NM_012573.4
Lipofectamine™ 3000 Transfection Reagent	ThermoFisher Scientific	L3000008
Software and algorithms		
MATLAB	MathWorks	N/A
Origin 2021 Pro	OriginLab	N/A
Clampfit 10.5	Molecular Devices	N/A
Imaris7	Bitplane	N/A
Spectronaut Pulsar	Biognosys	N/A
R	The R Foundation	N/A
WebGestalt	www.webgestalt.org	N/A
ImageJ 1.53v	https://imagej.nih.gov/ij	N/A
Chronux software package	http://chronux.org/[96]	N/A
Irregular-Resampling Auto-Spectral Analysis	IRASA[97]	N/A
NEURON simulation program version 7.7	neuron.yale.edu/neuron/	N/A
SPSS 27	IBM	N/A
Other		
Intraventricular bilateral cannula	PlasticsOne	model 3280PD2.0/SP
Osmotic pumps	Alzet	model 1002
Vibratome	Leica	VT 1200S
Examiner.Z1	Zeiss	N/A
P-87 pipette puller	Sutter instruments	N/A
Borosilicate glass, OD 1.5 mm, ID: 0.86 mm	Science Products	GB150F-10P
EPC 10 USB double amplifier/digitizer	HEKA	N/A
MultiClamp 700B	Molecular Devices	N/A
Axon Digidata 1550B digitizer	Molecular Devices	N/A
LSM 710	Zeiss	N/A
Leica TCS SP8	Leica	N/A
Zeiss Elyra 7	Zeiss	N/A

RESOURCE AVAILABILITY

Lead contact

Further information and requests for resources and reagents should be directed to and will be fulfilled by the lead contact, Christian Geis (christian.Geis@med.uni-jena.de).

Materials availability

Due to the finite available quantity, the patient material used in this study may be available on a limited basis from the lead contact with a completed Materials Transfer Agreement.

Data and code availability

- Statistical data associated with this study is presented in Table S1. Mass spectrometry proteomics data have been deposited at the ProteomeXchange Consortium via the PRIDE[95] partner repository and are publicly available at ProteomeXchange: PXD032055 via the following login credentials: username: reviewer_pxd032055@ebi.ac.uk; password: kPyDcasn. Accession numbers are listed in the key resources table. All proteomic data is available in Table S2.
- This paper does not report original code. Code associated with the neural network model is publicly available in ModelDB (https://senselab.med.yale.edu/ModelDB; accession number: 138421). MATLAB toolboxes for IRASA method (https://purr.purdue.edu/publications/1987/1), for multi-taper method (http://chronux.org), and for microglia analysis (https://github.com/isdneuroimaging/mmqt) are also available online.
- Any additional information required to reanalyze the data reported in this work paper is available from the lead contact upon request.

EXPERIMENTAL MODEL AND STUDY PARTICIPANT DETAILS

Animal model of NMDAR-encephalitis

Forty male C57BL/6J mice were housed in a room maintained at a controlled temperature of (21 ± 1°C) and humidity (55 ± 10%) with illumination at 12-h cycles; food and water were available *ad libitum*. Animal experiments were performed in accordance with the ARRIVE guidelines for reporting animal research[98] and the experimental protocol was in accordance with European regulations (Directive 2010/63/EU) and was approved by the local animal welfare committee (Thüringer Landesamt für Lebensmittelsicherheit und Verbraucherschutz, 02–059/13 and UKJ-23-002). Sixteen-weeks old (25-30g) mice were implanted with biventricular osmotic pumps (model 1002, Alzet, Cupertino, CA) with the following characteristics: volume 100 μL, flow rate 0.25 μL/h, and duration 14 days, as previously reported.[61,99] The day before surgery the two pumps were each filled with 100μL of 1μg/μL human monoclonal NMDAR-Ab (#003–102) or Control-Ab (#mGO53).[25] Alternatively, for some experiments undiluted patient CSF was used from a patient with NMDAR-encephalitis and from a control patient without encephalitis (see below).

Mice under isoflurane anesthesia were placed in a stereotactic frame, and a bilateral cannula (model 3280PD2.0/SP, PlasticsOne) was inserted into the ventricles (coordinates: 0.2 mm posterior and ±1.00 mm lateral from bregma, depth 2.2 mm). The cannulas were connected to two subcutaneously implanted osmotic pumps on the back of the mice.

Patient material

NMDAR-CSF from a patient with autoimmune NMDAR encephalitis was tested using a commercial cell based assay (Euroimmun, Lübeck, Germany; titer) and revealed a high titer of 1:100. Patient CSF (NMDAR-CSF) and Control-CSF from a patient with normal pressure hydrocephalus was also tested using HEK293 cells transfected with GluN1-eGFP and GluN2A subunits of the NMDAR (NR1a:GFP pEGFP-N3; NR2A pRK7) using Lipofectamine 3000 (ThermoFisher Scientific, MA, USA) primary and vital mouse embryonic hippocampal neurons (d.i.v. 14), and acute mouse hippocampal cryosections (10 μm). NMDAR-CSF, but not Control-CSF showed strong staining of transfected HEK cells, revealed characteristic synaptic staining pattern in primary neurons and mouse hippocampal cryosections (Figure S9). Primary antibody: IgG 003–102 (mAb against GluN1), Control CSF- and NMDAR-CSF; secondary antibody: goat anti-human Cy3. The use of patient CSF biomaterial was approved by the Jena University Ethics Committee (# 2019-1415-Material) and patients provided informed consent.

METHOD DETAILS

Acute hippocampal preparation

Two weeks (14–16 days) after intraventricular osmotic pump implantation, mice were deeply anesthetized with Isoflurane, decapitated, and the brain was removed in ice-cold protective artificial cerebrospinal fluid solution (paCSF) containing, in mM: 95 N-Methyl-D-Glucamine, 30 NaHCO$_3$, 2.5 KCl, 1.25 NaH$_2$PO$_4$, 10 MgSO$_4$, 0.5 CaCl$_2$, 20 HEPES, 25 glucose, 2 thiourea, 5 Na-ascorbate, 3 Na-pyruvate, 12 N-acetylcysteine, adjusted to pH 7.3 and 300–310 mOsmol, saturated with Carbogen. Hippocampal 350μm-thick transverse slices were prepared on a vibratome (VT 1200S, Leica, Wetzlar, Germany) in ice-cold paCSF and transferred for warm recovery in paCSF at 32°C for 12 min. Before recordings, slices were left to recover for at least 60 min at room temperature in aCSF+ containing in mM: 125 NaCl, 25 NaHCO$_3$, 2.5 KCl, 1.25 NaH$_2$PO$_4$, 1 MgCl$_2$, 2 CaCl$_2$, 25 glucose, 2 thiourea, 5 Na-ascorbate, 3 Na-pyruvate, 12 N-acetylcysteine, adjusted to pH 7.3 and an osmolarity of 300–310 mOsmol, and saturated with Carbogen. For recordings, slices were transferred in a recording chamber under continuous perfusion (2–4 mL/min, Ismatec, Wertheim, Germany) with 27°C aCSF containing in mM 125 NaCl, 2.5 KCl, 25 NaHCO$_3$, 1.25 NaH$_2$PO$_4$, 1 MgCl$_2$, 2CaCl$_2$, saturated with Carbogen.

Whole-cell recordings

Researchers performing all recording experiments and analyses were blinded to the experimental treatment of the animals. CA1 pyramidal neurons (CA1-PN) were visually identified using a microscope (Examine.Z1, Zeiss, Jena, Germany) equipped with differential interference contrast optics. Patch pipettes were pulled using a P-87 horizontal pipette puller (Sutter Instruments, Novato, CA, USA) from thick-walled borosilicate glass (0.86x1.50, Science Products, Kamenz, Germany) and had a resistance of 2.5–5 MΩ when filled with intracellular solutions. For voltage-clamp recordings, the intracellular solution contained in mM 135 CsMeSO$_4$, 3 CsCl, 10 HEPES, 0.2 EGTA, 0.1 spermine, 2 QX-314-Br, 2 Mg$_2$-ATP, 0.3 Na$_2$-GTP, 10 phosphocreatine (pH 7.25, osmolarity 280 mOsmol), while for current-clamp recordings the intracellular solution contained in mM 150 K-Gluconate, 1.5 MgCl$_2$, 10 HEPES, 0.2 EGTA, 0.1 spermine, 2 Mg$_2$-ATP, 0.3 Na$_2$-GTP, 10 phosphocreatine (pH 7.25, osmolarity 280 mOsmol). For morphological reconstructions 3 mg/ml biocytin was freshly added to the intracellular solutions before recordings. During voltage-clamp recordings, 1μM AM-251 was added to aCSF to block depolarization-induced suppression of inhibition.[32] For field potential measurements, the recording electrode was filled with aCSF.

Voltage-clamp (Vc) and current-clamp (Ic) signals were recorded and digitized with an EPC 10 USB double amplifier/digitizer (HEKA, Ludwigshafen/Rhein, HRB 41752) or recorded with a MultiClamp 700B amplifier (Molecular Devices, Sunnyvale, CA, USA), and digitized using an Axon Digidata 1550B digitizer (Molecular Devices, Sunnyvale, CA, USA). Signals were low-pass filtered at 2kHz (Vc) or 5kHz (Ic) and digitized at 20kHz. Data acquisition was performed in PatchMaster v2x80 (HEKA, Ludwigshafen/Rhein, HRB 41752) or Clampex 10.7 (Molecular Devices, Sunnyvale, CA, USA). Measured and applied potentials were corrected online for an experimentally determined liquid junction potential of 8mV for both intracellular solutions. Recording of the resting membrane potential was performed immediately after break-in, and cells with a membrane potential higher than −60mV were discarded. Series resistances (<25MΩ) was 70% compensated and was monitored throughout recordings. Cells were discarded if a >20% change in series resistance occurred. Analysis of recorded signals was performed in Clampfit 10.7 (Molecular Devices, Sunnyvale, CA, USA) or in MATLAB (MathWorks) using custom-written code (see below).

Stimulation of the Schaffer collaterals (SC) was performed with an aCSF-filled micropipette acting as a monopolar stimulation electrode that was placed 200–300μm away from the recording electrode. Stimulation was applied through a constant current stimulation unit (DS3, Digitimer) for 40 μs at an intersweep frequency of 0.1Hz. The reversal potentials of synaptic excitation and inhibition were measured after bath application of 100μM PTX (for $E_{excitation}$) or 10μM CNQX and 50mM AP-5 (for $E_{inhibition}$), after which CA1-PN were recorded at different holding potentials during single SC stimulation (Figure S2A). The reversal potentials were measured as −5 mV and −70 mV for excitation and inhibition, respectively.

To determine the synaptic input/output (I/O) curves of CA1-PN, recorded cells in Ic mode were held at 0pA while SC were stimulated at incremental strengths at 0.1Hz until action potential (AP) probability reached 100% (ca. 80–100 sweeps). EPSP slopes were binned, and AP probability was determined per bin.[23] To determine the input resistance, we calculated the slope of a straight-line fit to the voltage-current curve which was established using subthreshold current injections. The membrane time constant was measured by fitting a single exponential to the voltage response of a −20pA current step. Voltage sag and APs were elicited by current step injections from −240pA to 360pA in 20 pA steps. AP threshold was defined as the potential at which the rise slope exceeded 15V/s.[100] The spike frequency adaptation was calculated as the ratio of the last interspike interval to the first one. EPSP jitter was calculated as the SD of EPSP latency at I/O threshold. AP jitter was calculated as the SD of the AP latency at twice the I/O threshold slope or at 10V/s, whichever was lower.

The impedance amplitude profile (ZAP) was determined by injecting a 20s-long, linearly increasing chirp current (0-15Hz) from a baseline of 0pA (at resting potential). The amplitude of the injected current was adjusted to evoke a subthreshold, ∼10mV peak-to-peak response. Following previous studies,[101,102] we calculated ZAP as a function of the input frequency $Z(f) = \tilde{V}(f)/\tilde{I}(f)$, where $\tilde{V}(f)$ and $\tilde{I}(f)$ are the fast Fourier transform (fft) of the cell membrane potential V and the applied chirp current I. Both V and I were downsampled to 2 kHz prior to fft. $Z(f)$ is a complex number and its absolute value determines the impedance amplitude at frequency f, denoted as $|Z(f)|$. In our results we refer to $|Z(f)|$ as the impedance. For each cell, we computed $|Z(f)|$ for each sweep (out of 3) separately, then averaged across the trials.

To evoke biphasic (eEPSC-eIPSC) and monophasic (eEPSC or eIPSC) responses, SC were incrementally stimulated and eEPSCs were recorded at a holding potential of −70mV until a plateau potential was reached (eEPSC's I/O curve). Thereafter, supramaximal stimulation intensity was used. Biphasic responses were elicited by changing the holding potential to approx. −35mV and optimizing the holding potential for a maximal amplitude of both components (range −40mV to −25mV). Short-term plasticity was investigated by applying paired-pulse supramaximal stimulation of the SC at 50ms and 200ms intervals, and train stimulation by applying a 100-pulse train of supramaximal stimulation of the SC at 20Hz. The excitatory integration window was measured as the time interval between the peak of the excitatory (eEPSC) and the peak of the inhibitory (eIPSC) components in biphasic responses.

Local field potentials (LFP) were recorded only using a MultiClamp700B with the headstage in voltage-follower mode, with a low-pass Bessel filter of 1kHz and a sampling frequency of 20kHz. For electrically evoked oscillations, the recording electrode, consisting of a micropipette (∼2MΩ) filled with aCSF, was placed in the stratum pyramidale of the hippocampal CA1 region, while the stimulus electrode was placed 200-300μm away in the stratum radiatum toward the CA3. Supramaximal stimulation (1000μA) of the SC at 100Hz was repeated for three sweeps (60s intersweep interval). For chemically evoked oscillations, we prepared 400μm thick

horizontal hippocampal slices to promote oscillatory activity in slices,[103] and baseline LFP was measured for 5 min, before adding 20μM carbachol or 20μM carbachol with 10μM LY404187 (AMPA-PAM, Tocris Bioscience, Bristol, UK) to the bath solution, after which LFP was measured for 7 min.

Analysis of synaptic currents was performed in Clampfit 10.5 using the template search function. Templates of spontaneous excitatory and inhibitory postsynaptic currents (sEPSC and sIPSC, respectively) were obtained by averaging 25–35 manually-selected events per group. All events with a detection similarity threshold of three were further verified by visual inspection. Decay time constants were estimated by a single exponential fit. The median was used to calculate the central tendency of synaptic parameters per cell (sEPSC/sIPSC amplitude, frequency, decay tau, charge transfer).

Biocytin staining and morphologic analysis

After recording, slices were transferred in 4% PFA and fixed overnight at 4°C. After washing in TBS, slices were incubated for 2 h in TBS plus (TBS, 5% donkey serum, 0.3% Triton X-100) and then incubated overnight in 1:500 Streptavidin-Cy3 (Sigma) in TBS plus before embedding in Entellan (Merck, Darmstadt, Germany). Filled neurons were captured on a confocal scanning microscope (LSM 710, Zeiss, Jena, Germany) and morphologic analysis was performed in Imaris7 (Bitplane, Belfast, UK).

Sample preparation for proteomics

Immediately after decapitation, hippocampi (10/group) were dissected and flash-frozen at −40°C and subsequently stored at −80°C. Hippocampi were thawed and transferred into Precellys lysing kit tubes (Keramik-kit 1.4/2.8 mm, 2 mL (CKM)) containing 200 μL of PBS supplemented with 1 tab of cOmplete, Mini, EDTA-free Protease Inhibitor per 50 mL. For homogenization, tissues were shaken twice at 6000 rpm for 30 s using Precellys 24 Dual (Bertin Instruments, Montigny-le-Bretonneux, France) and the homogenate was transferred to new 1.5 mL Eppendorf tubes. For each sample, 100 μL of homogenate was diluted with 2x lysis buffer (final concentrations: 2% SDS, 100 mM HEPES, pH 8.0), sonicated in a Bioruptor Plus (Diagenode, Seraing, Belgium) for 10 cycles with 1 min ON and 30 s OFF with high intensity at 20°C, and then heated at 95°C for 10 min. A second sonication cycle was performed as described above. Lysates were stored at −80°C until further processing.

Lysates were thawed, sonicated as described above, and aliquots corresponding to 100 μg of protein were reduced using 10 mM DTT for 30 min at room temperature and alkylated using freshly made 15 mM IAA for 30 min at room temperature in the dark. Subsequently, proteins were acetone precipitated and digested using LysC (Wako sequencing grade) and trypsin (Promega sequencing grade), as described by.[104] The digested proteins were then acidified with 10% (v/v) trifluoracetic acid and desalted using *Waters Oasis HLB μElution Plate 30 μm* following manufacturer instructions. The eluates were dried down using a vacuum concentrator and reconstituted in 5% (v/v) acetonitrile, 0.1% (v/v) formic acid. For mass spectrometry (MS) analysis, samples were transferred to an MS vial, diluted to a concentration of 1 μg/μL, and spiked with iRT kit peptides (Biognosys, Zurich, Switzerland) prior to analysis.

Proteomics data acquisition

Approximatively 1μg of reconstituted were separated using a nanoAcquity UPLC (Waters, Milford, MA) was coupled online to the MS. Peptide mixtures were separated in trap/elute mode, using a trapping (Waters nanoEase M/Z Symmetry C18, 5μm, 180 μm × 20 mm) and an analytical column (Waters nanoEase M/Z Peptide C18, 1.7μm, 75 μm × 250 mm). The outlet of the analytical column was coupled directly to an Orbitrap Fusion Lumos mass spectrometers (Thermo Fisher Scientific, San Jose, CA) using the Proxeon nanospray source. Solvent A was water, 0.1% formic acid and solvent B was acetonitrile, 0.1% formic acid. The samples were loaded with a constant flow of solvent A, at 5 μL/min onto the trapping column. Trapping time was 6 min. Peptides were eluted via the analytical column with a constant flow of 300 nL/min. During the elution step, the percentage of solvent B increased in a nonlinear fashion from 0% to 40% in 120 min. Total runtime was 145 min, including cleanup and column re-equilibration. The peptides were introduced into the mass spectrometer via a Pico-Tip Emitter 360 μm OD x 20 μm ID; 10 μm tip (New Objective) and a spray voltage of 2.2 kV was applied. The capillary temperature was set at 300°C. The RF lens was set to 30%. Full scan MS spectra with mass range 350–1650 m/z were acquired in profile mode in the Orbitrap with resolution of 120,000 FWHM. The filling time was set at maximum of 20 ms with an AGC target of 5×10^5 ions. Data Independent Acquisition (DIA) scans were acquired with 40 mass window segments of differing widths across the MS1 mass range. The HCD collision energy was set to 30%. MS/MS scan resolution in the Orbitrap was set to 30,000 FWHM with a fixed first mass of 200m/z after accumulation of 1×10^6 ions or after filling time of 70ms (whichever occurred first). Data were acquired in profile mode. For data acquisition and processing Tune version 2.1 and Xcalibur 4.1 were employed.

Proteomics data analysis

Raw DIA files were analyzed in directDIA mode using Spectronaut Pulsar (v15, Biognosys, Zurich, Switzerland). The data were searched against a species-specific protein database (Uniprot *Mus musculus* release 2016_01) with a list of common contaminants. The data were searched with the following modifications: carbamidomethyl (C) as fixed modification, and oxidation (M) and acetyl (protein N-term) as variable modifications. A maximum of 2 missed cleavages was allowed. The search was set to 1% false discovery rate (FDR) at both protein and peptide levels. DIA data were then uploaded and searched against this spectral library using Spectronaut Professional (v.15) and default settings. Relative quantification was performed in Spectronaut for each pairwise comparison using the replicate samples from each condition using default settings, except: Major Group Quantity = median peptide quantity; Major Group Top N = OFF; Minor Group Quantity = median precursor quantity; Minor Group Top N = OFF; Data Filtering = Q value; Normalization

Strategy = Local normalization; Row Selection = Automatic; Exclude Single Hit Proteins = TRUE. Differential abundance testing was performed using an un-paired t test between replicates. p values were corrected for multiple testing multiple testing correction with the method described by.[105] The data (candidate table) and protein quantity data report were exported, and further data analyses and visualization were performed with R (v.4.0.5) and R studio server (v. 2022.02.0) using in-house pipelines and scripts. KEGG pathway and Gene Ontology over-representation analyses were performed with WebGestalt[106] using the significant protein groups (q < 0.05) against a background of all the quantified protein groups. Significantly enriched pathways and GO terms were defined using a cut-off of FDR <0.05.

Histological analysis of mouse brain sections
Perfusion and brain sectioning
18 days after pump implantation and intraventricular transfer of NMDAR-mAb or Control-mAb (100 μg/ml), mice were anesthetized with 5% isoflurane and intracardially perfused wit 4% paraformaldehyde (PFA). Brains were gently removed and postfixed in 4% PFA for 24 h. Brains were cut on a vibratome into 100 μm thick coronal sections for microglia morphology analysis, and into 40 μm thick coronal slices for Iba1/CD68 and CD3 stainings.

Immunostaining
Successful human IgG infusion was confirmed by staining against the human IgG (goat anti human 633, A-21091, Invitrogen, concentration 1 : 500) on free floating sections at 4° overnight. Microglia were stained using anti-Iba-1 antibody (rabbit, 1:500, Wako, #019–19741) combined with a secondary antibody (goat anti rabbit, 1:500, A23733, Thermofisher). For analysis of microglia activation, we used anti-CD68 antibody (rat, 1:500, BioRad, 1:500, #MCA1957) combined with a secondary antibody (donkey anti rat, 1:500, AF647, Jackson, #712-606-150). For CD3 staining we used anti-CD3 antibody (rat, 1:200, BioLegend, #100201) combined with a secondary antibody (goat anti rat, 1:500, AF488, Invitrogen, #A11006).

Confocal microscopy of microglia
Images were acquired at a confocal microscope (Leica TCS SP8) with a 40× objective at a resolution of 1024× 1024 pixels (pixel dimensions in x and y 0.2μm, covering 205 × 205 μm) at z increments of 0.4μm.

Analysis of microglia
To extract the morphological parameters of microglia we subjected the acquired confocal imaging stacks to an automated image analysis pipeline.[39] The MATLAB scripts can be downloaded at https://github.com/isdneuroimaging/mmqt. Using this pipeline we extracted the number of segments per main branch, branch length, circularity, and betweennes, as detailed in.[39] Of note, the betweenness is a graph-theory measure employed here to quantify the complexity of microglia processes. In brief, betweenness measures the extent to which a node (here, a microglial segment) acts as a hub or bridge connecting different nodes in the network (here, of the segments).

Acquisition and analysis of CD68/Iba1 and CD3 immunostainings
Widefield fluorescence imaging of the CA1 region of the hippocampus was performed on a ZEISS Elyra 7 system. Analysis was performed in ImageJ 1.53v (https://imagej.nih.gov/ij/).

Analysis of electrically induced oscillations
The HFS-induced network oscillations were recorded as described above. The signals were then processed using custom written code in MATLAB (MathWorks). For a proper time-frequency analysis, while reducing the potential stimulus-induced edge-like effects (see below), we subjected each HFS signal to the following correction steps and verified the results visually. (1) The baseline of the before-stimulus section of the signal (~2.15 s) was corrected using the robust polynomial fitting method of maximum 7th-order. (2) The sharply increasing baseline of the signal, observed right after the stimulus offset (see results), was removed using a polynomial of 17th order. To avoid the disturbance of the signal dynamics by this high-order polynomial, we applied this fitting to only 2.1 s of the after-stimulus signal. Note that we also considered the 10 ms after the last impulse of HFS as a part of stimulus duration, in order to avoid the introduction of stimulus artifact in our results. (3) Using the same procedure as in step (1), we removed the baseline of the remaining (tail) of the signal after stimulus. (4) The 200-milliseconds stimulus artifact was replaced with the mirrored version (along y axis) of the first 200-milliseconds of the baseline-corrected HFS signal generated in step 2; note, the time is considered as x axis. (5) Finally, the baseline-corrected HFS signal was obtained by concatenating the resulted signals in steps 1–4. To extract the local field potential (LFP) activity this signal was then digitally band-pass filtered in the range of 1.1–250 Hz using a Kaiser window finite impulse response filter (KW-FIR) with a sharp transition band bandwidth of 1 Hz, stopband attenuation of 60 dB, and passband ripple of 1%. To avoid the potential edge effects of the signal due to the filtering a mirrored version of the whole signal was appended to the beginning and the end of the signal, prior to the filtering. These copies were cut out of the filtered signal afterward.

To characterize the transient gamma oscillations induced by the HFS we used the time-frequency analysis of the resultant baseline-corrected LFP signals. We performed this analysis separately for the first ~2.15 s part of the signal before stimulus onset (bLFP) and the last ~7.6 s of the signal after the stimulus offset (aLFP). To this end, we convolved each signal with the complex Morlet wavelets of frequencies from 4 to 110 Hz with the increment of 0.5 Hz. As the wavelet scales we used the number of cycles from 5 to 10 (logarithmically-spaced over these frequency levels) thereby effectively accounting for the time-frequency resolution trade-off of the wavelet transforms. For each level of wavelet scale (or frequency), the LFP power at each time point was computed as the squared magnitude of the corresponding coefficient of the wavelet transform at each time-frequency pair; $P_{bLFP}(t,f)$ and $P_{aLFP}(t,f)$. The edge

effects in the transform results were considered as missing values, and thus discarded. In the case of aLFP signal, we considered the stimulus duration, which we replaced using the mirrored aLFP signal (see above), as a part of aLFP. This enabled us to shift the left edge effect to the onset of stimulus, and thus have the wavelet transform of aLFP almost free of this edge effect. The mirrored part (i.e., of stimulus duration) was then cut out of the wavelet results. To minimize the effect of potential 1/f power scaling phenomenon as well as e.g., the slice- and electrode-specific idiosyncratic characteristics we computed the relative power values:

$$P_{rel}(t,f) = \frac{P_{aLFP}(t,f) - \overline{P_{bLFP}(f)}}{\overline{P_{bLFP}(f)}}$$

Where, $P_{rel}(t,f)$ denotes the induced power after the stimulus at time t and frequency level f, and $\overline{P_{bLFP}(f)}$ denotes the time-averaged power of the bLFP at f.

To investigate the evolution of induced gamma power over time we computed the total instantaneous power as the mean of $P_{rel}(t,f)$ over 30–90 Hz (gamma band) at each t. To show that our findings are not affected by the normalization we also computed the raw (i.e., non-normalized) total instantaneous power as the mean of $P_{aLFP}(t,f)$ over 30–90 Hz at each t. To investigate the frequency components of the induced power (i.e., power spectrum) we computed the mean of $P_{rel}(t,f)$ over 400 ms after the stimulus offset at each f. Note that this selected window size effectively captures the induced transient gamma responses, before returning to the baseline (see results). We repeated all these analyses for each sweep (out of three) of the recording session, and then averaged the results over the sweeps to increase the signal-to-noise ratio. For testing the mean difference in gamma power between the two groups (Control vs. NMDAR-Ab) over time, we considered 1.6 s of the total instantaneous gamma power time-series after the stimulus offset and divided it to non-overlapping 200-milliseconds bins. We then performed a two-tailed permutation test with 1,000,000 times shuffling at a significance level of 5% while accounting for the multiple-comparison problem by the method of Cohen.[107]

In our preliminary analysis we found that HFS not only induces strong gamma oscillations but also some relatively weak theta responses. Using Chronux software package (http://chronux.org/),[96] we applied the multi-taper method (time-bandwidth product of 2 with 3 tapers) to the first 500-milliseconds of each aLFP (1.1–250 Hz), in order to first compute the power spectrum of the theta responses. We then assessed how these two responses were coordinated in time using the theta-gamma co-modulation index (TGC).[108] To this end, we band-pass filtered the baseline-corrected HFS signal using the same KW-FIR filter as above but in the range of 30–90 Hz (for gamma band) and 5–12 Hz (for theta band), separately. This was followed by applying the Hilbert transform and computing the magnitude (i.e., amplitude envelop) of these band-specific signals at each time point, using the resulted analytic signals. This was followed by binning the first 450-milliseconds of these signals using a sliding window of 200 ms size with a step size of 50 ms. The selected bin size was sufficiently large to enclose ∼1–2.5 and ∼6–18 cycles of theta (5–12 Hz) and gamma oscillations (30–90 Hz), respectively (see results). TGC was then computed as the Pearson correlation between the magnitude time-series of the theta- and gamma-band signals at each bin. To compare the TGC of the groups at the center of each of 5 bins we used the same permutation-test of Cohen[107] mentioned above.

As an alternative analysis to assess the temporal characteristics of the induced oscillations, we used autocorrelation function (ACF); a measure of the similarity between the values of the same signal over successive time intervals. To do this, for each baseline-corrected LFP signal (5–120 Hz), we computed ACF for 800-milliseconds of its aLFP and of its corresponding bLFP signal preceding the stimulus onset. To compute the induced ACF we then subtracted ACF of the baseline from that of after-HFS.

Analysis of chemically induced oscillations

The LFP signals under chemical stimulation were recorded as described above. These signals were then processed using custom written code in MATLAB (MathWorks). The artifacts were identified by visual inspection and excluded. To extract LFP activity both properly and in a computationally efficient manner, each signal was subjected to the following processing steps. (1) The signal was downsampled to 10 kHz. (2) It was then digitally low-pass filtered using a KW-FIR filter with a passband cutoff of 1 kHz, stopband band of 50 Hz, stopband attenuation of 60 dB, and passband ripple of 1%. (3) This was followed by a downsampling to 5 kHz. (4) Finally, the LFP signal was obtained by band-pass filtering the resulted signal using the same KW-FIR filter as used for HFS data (see above) but in the range of 2–250 Hz.

Field potential signal are usually composed of both fractal (aperiodic or 1/f noise) and oscillatory (periodic) dynamics, governed presumably by distinct biological mechanisms. In this work, we are interested in investigating the potential changes in the neural oscillations due to NMDAR-Ab. Hence, in order to separate these components in the power spectrum of the LFP signals we used the Irregular-Resampling Auto-Spectral Analysis (IRASA) method.[97] This enabled us to assess the power characteristics of the oscillatory dynamics in LFP signals exclusively, i.e., without being affected by that of the 1/f noise. When applying IRASA to each LFP signal we used a sliding window of 1-s size with 50% overlap. We used the same steps to obtain the LFP signals and the corresponding power spectrums for 10-min recorded signals under Carbachol+PAM application.

Computational neural network model

To gain mechanistic insights into the mechanism underlying the abnormal increase in gamma oscillations due to NMDAR-Ab we used computational modeling. To do this, we employed a well-established biophysical recurrent neural network model of CA1.[43,44,103] The model is amenable to reproduce the hippocampal theta-nested gamma oscillations, and has been used extensively in previous studies

to explain, or predict, the dynamics of the experimentally observed oscillatory dynamics in LFP signals under various behavioral or pharmacological conditions.[43–45,103,109] As compared to the mean-filed CA1 network models,[81,110,111] this model allows for investigating the network dynamics using a more detailed parameterization of biophysical parameters at both synaptic and single-cell levels. To set the parameter values of this model, we mainly followed previous studies,[43,44] and considered the resulted model as representing the Control group in our data. We then emulated the NMDAR-Ab condition by applying the relative changes in synaptic and cellular parameter values of the model, according to our measurements (Figures 1, 2, and 3). The list of the percentage changes used in the NMDAR-Ab model, relative to Control model, can be found in Table S3. By analyzing the simulated LFP (simLFP) and spike rastergrams, we then sought to mechanistically address the mechanism and parameter changes mediating the increase in gamma in NMDAR-AB group.

The model is consisted of the single compartment, Hodgkin-Huxley-type neuron models of pyramidal cells ("E cells"; excitatory), fast spiking PV$^+$ cells ("I cells"; inhibitory), and oriens lacunosum-moleculare interneurons cells (O-LM or "O cells"; inhibitory). Similarly to previous studies,[43,44] we modeled E-population as a single cell which fires at the population frequency thereby generating EPSPs in the I (n = 10) and O (n = 10) cells at the gamma frequency, as observed experimentally.[46] In our model, we assumed that the E and I cells receive also external constant (with additive noise) excitatory drive through Schaffer collaterals (SC). However, in general, this drive current can be considered to be delivered by pathways other than SC, like temporoammonic (EC→CA1). In the following, we describe the corresponding neuron and synaptic models, LFP model and its analysis, and the steps used for setting the numeric and random aspects of the model.

Neuron models

E cell: For the pyramidal cell, we use Olufsen et al.[112] model, as a variation of Ermentrout et al.[113] model,:

$$C\frac{dV}{dt} = g_{Na}m_\infty(V)^3h(V_{Na} - V) + g_Kn^4(V_K - V) + g_L(V_L - V) + I \quad \text{(Equation 1)}$$

$$\frac{dh}{dt} = \frac{h_\infty(V) - h}{\tau_h(V)} \quad \text{(Equation 2)}$$

$$\frac{dn}{dt} = \frac{n_\infty(V) - n}{\tau_n(V)} \quad \text{(Equation 3)}$$

With

$$x_\infty(V) = \frac{\alpha_x(V)}{\alpha_x(V) + \beta_x(V)} \text{ for } x = m, h, \text{ or } n \quad \text{(Equation 4)}$$

$$\tau_x(V) = \frac{1}{\alpha_x(V) + \beta_x(V)} \text{ for } x = h \text{ or } n \quad \text{(Equation 5)}$$

$$\alpha_m(V) = \frac{0.32(V+54)}{1 - \exp(-(V+54)/4)}$$

$$\beta_m(V) = \frac{0.28(V+27)}{\exp((V+27)/5) - 1}$$

$$\alpha_h(V) = 0.128 \exp(-(V + 50)/18)$$

$$\beta_h(V) = \frac{4}{1 + \exp(-(V+27)/5)}$$

$$\alpha_n(V) = \frac{0.032(V+52)}{1 - \exp(-(V+52)/5)}$$

$$\beta_n(V) = 0.5 \exp(-(V + 57)/40)$$

In Equations 1, 2, and 3, the letters C, V, t and τ, g, and I denote capacitance density, voltage, time, conductance density, and current density, respectively. The units that we use for these quantities are μF/cm^2, mV, ms, mS/cm^2, and μA/cm^2. For brevity, units will

usually be omitted hereafter. The parameter values of the model are $C = 1$, $g_{Na} = 100$, $g_K = 80$, $g_L = 0.1$, $V_{Na} = 50$, $V_K = -100$, and $V_L = -67$.

I cells: For fast-spiking PV + interneurons, we use the model described in Wang and Buzsáki.[114] Equations 1, 2, 3, and 4 are the same as in the E cell model, but the Equation 5 is replaced by:

$$\tau_x(V) = \frac{0.2}{\alpha_x(V) + \beta_x(V)} \text{ for } x = h \text{ or } n$$

with the rate functions α_x and β_x ($x = m, h,$ and n) are defined as follows:

$$\alpha_m(V) = \frac{0.1(V+35)}{1 - \exp(-(V+35)/10)}$$

$$\beta_m(V) = 4\exp(-(V + 60)/18)$$

$$\alpha_h(V) = 0.07\exp(-(V + 58)/20)$$

$$\beta_h(V) = \frac{1}{\exp(-0.1(V+28))+1}$$

$$\alpha_n(V) = \frac{0.01(V+34)}{1 - \exp(-0.1(V+34))}$$

$$\beta_n(V) = 0.125\exp(-(V + 44)/80)$$

The parameter values, using the same units as for the pyramidal cell, are $C = 1$, $g_{Na} = 35$, $g_K = 9$, $g_L = 0.1$, $V_{Na} = 55$, $V_K = -90$, and $V_L = -65$.

O cells: For the oriens lacunosum-moleculare (O-LM) interneurons, we use the model described in Tort et al.,[109] which is a reduction of the multi-compartmental model described in Saraga et al.[115] The current-balance equation is given by:

$$C\frac{dV}{dt} = g_{Na}m^3h(V_{Na} - V) + g_K n^4(V_K - V) + g_A ab(V_A - V)$$
$$+ g_h r(V_h - V) + g_L(V_L - V) + I$$

(Equation 6)

With

$$\frac{dx}{dt} = \frac{x_\infty(V) - x}{\tau_x(V)} \text{ for } x = m, h, n, a, b, r$$

(Equation 7)

For $x = m, n, h$, the functions $x_\infty(V)$ and $\tau_x(V)$ are the same as in Equations 4 and 5, and the rate functions α_x and β_x are defined as follows:

$$\alpha_m(V) = \frac{-0.1(V+38)}{\exp(-(V+38)/10) - 1}$$

$$\beta_m(V) = 4\exp(-(V + 65)/18)$$

$$\alpha_h(V) = 0.07\exp(-(V + 63)/20)$$

$$\beta_h(V) = \frac{1}{1+\exp(-(V+33)/10)}$$

$$\alpha_n(V) = \frac{0.018(V - 25)}{1 - \exp(-(V - 25)/25)}$$

$$\beta_n(V) = \frac{0.0036(V - 35)}{\exp((V - 35)/12) - 1}$$

For $x = a, b, r$, the functions $x_\infty(V)$ and $\tau_x(V)$ are defined as:

$$a_\infty(V) = \frac{1}{1+\exp(-(V+14)/16.6)}$$

$$\tau_a(V) = 5$$

$$b_\infty(V) = \frac{1}{1+0.07\exp((V+71)/7.3)}$$

$$\tau_b(V) = \frac{1}{\frac{0.000009}{\exp((V-26)/18.5)}+\frac{0.014}{0.2+\exp(-(V+70)/11)}}$$

$$r_\infty(V) = \frac{1}{1+\exp((V+84)/10.2)}$$

$$\tau_r(V) = \frac{1}{\exp(-14.59-0.086V)+\exp(-1.87-0.0701V)}$$

The parameter values, using the same units as for the pyramidal cell, are $C = 1.3$, $g_L = 0.05$, $g_{Na} = 30$, $g_K = 23$, $g_A = 16$, $g_h = 8$, $V_{Na} = 90$, $V_K = -100$, $V_A = -90$, $V_h = -32$, $V_L = -70$; see also Wulff et al.[43]

Synaptic model

Following previous studies,[43,44,113] we model each synaptic input as a current of the form $I_{syn,XY} = G_{XY}/N_X\, s(V - V_{syn})$, where X and Y denote the type of the pre and postsynaptic cell, respectively (i.e., X and Y $\in$ {E, I, O}), G_{XY} is the maximal synaptic conductance, N_X is the number of X cells, V is the membrane potential of the postsynaptic cell, and V_{syn} is the reversal potential. The variable s is a normalized double-exponential function characterized by rise ($\tau_{X,r}$) and decay ($\tau_{X,d}$) time constants. The synapses were implemented using the Exp2Syn() built-in function of NEURON. The IPSPs originating from the O cells synapses were slower than IPSPs originating from the I cells synapses; following these stuides, we used $\tau_{E,r} = 0.05$ ms and $\tau_{E,d} = 5.3$ ms for E synapses, $\tau_{I,r} = 0.07$ ms and $\tau_{I,d} = 9.1$ ms for I synapses, and $\tau_{I,r} = 0.2$ ms and $\tau_{I,d} = 22$ ms for O synapses. The reversal potential was set to 0 mV for E synapses and to -80 mV for I and O synapses. We used $G_{II} = 0.01$, $G_{OI} = 0.15$, $G_{IO} = 0.2$, $G_{IE} = 0.1$, $G_{OE} = 0.12$, $G_{EI} = 0.05$, $G_{EO} = 0.09$. In our model, in addition to the synaptic inputs ($I_{syn,XY}$) from X populations within CA1, the cells receive also some external drive currents, e.g., from other hippocampus regions or stimulus. We model this drive as having a constant (i.e., mean) level of ε_X with an additive white noise. Here, we set $\varepsilon_E = 2$, $\varepsilon_I = 0.3$, and $\varepsilon_O = 0$. Here, for the E and I cells, ε_E and ε_I represent the mean excitatory drive currents to E and I populations through SC pathway, hence, hereafter, we denote them by $\varepsilon_{SC,E}$ and $\varepsilon_{SC,I}$, respectively. Using these drive currents, which are in consistent with previous studies,[43,44,109] simLFPs of Control model presented theta and gamma peak frequencies at $\sim$8–10 Hz and $\sim$48–50 Hz, respectively. Of note, the model gamma peak frequency provides a compromise between those we observed in HFS- and CCH-induced gamma oscillations (see results).[40,47] The model theta peak frequency also closely reproduces that in our data (see results).

Model local field potential

The simulated local field potential (simLFP) of the model consisted of the membrane potential of a "passive" E cell programmed inside the network[43,44,109] This cell receives the same synaptic inputs as the "active" E cell. However, this cell does not send any synaptic output onto other cells and, in addition, it also does not spike given that its external drive current is set to zero. Power spectra of the simLFP was obtained using the Welch's method (MATLAB *pwelch()* function) with 0.2 s Hamming windows, 75% overlap. In the preliminary analysis, we found that our findings hold true also for larger window sizes. However, our chosen window size was able to provide a clear visualization of the main results, by diminishing the potential harmonics of the theta and gamma rhythms. Accordingly, to show the average power spectrums and to readout the peak power robustly from simLFPs we used a window of 0.2 s size, and to extract the information about the exact peak frequency of the simLFPs we used a window of 2 s size (see results); see also Tort et al.[109]

Numeric and random aspects of model

All simulations were carried out using NEURON simulation program version 7.7 (https://www.neuron.yale.edu/neuron/).[116] The model is publicly available code in ModelDB (https://senselab.med.yale.edu/ModelDB; accession number: 138421), and was simulated with a time step of 25 μs. As initial conditions, the membrane potential of each cell was uniformly distributed between −85 and

−60 mV and the channel-gating variables were set to their corresponding steady-state values. Each cell was further randomized using a clamping current (I_{Clamp}) of random uniform magnitude and random uniform duration between 0 and $t_{syn}/2$, where $t_{syn} = 0.5$ s is the time when synapses were turned on. In addition to the drive current (see previous section), each cell in the network also received additive white noise current inputs; see also Dugladze et al. and Tort et al.[45,109] For each of the Control and NMDAR-Ab models (see Table S3), we simulated the model for 50 trials of 12 s and used the last 10 s of simLFPs for the analysis. Note that, in simLFP signals, the mentioned randomizations, together with the stochastic components of the drive currents, varied the exact theta and gamma peak frequencies as well as their harmonics from trial to trial thereby yielding the broadening of the peak frequencies by ∼2 Hz in the trial-averaged spectrum results (see results).

Modulation of network oscillations

Our model revealed an increase in θ- and to a lesser degree in γ-oscillations after implementing the NMDAR-induced reduction in $\varepsilon_{SC,E}$ individually (see model 3 in Figure 6D). To evaluate the potential compensatory role of the reduction in decay time constants of synaptic inhibition mediated by O-cells ($\tau_{O,d}$) and I-cells ($\tau_{I,d}$) we computed the power modulation parameter (Figure 6F):

$$M_j^r(\tau_{O,d}, \tau_{I,d}) = -\frac{\left(P_j^r - P_{Ctrl}^r\right) - \left(P_3^r - P_{Ctrl}^r\right)}{P_{Ctrl}^r - P_3^r} = \frac{P_j^r - P_3^r}{P_3^r - P_{Ctrl}^r}$$

Where, $r \in \{\theta, \gamma\}$, P_j^r is the peak power of r-type oscillations ($r \in \{\theta, \gamma\}$) in model j, where j refers to using different set of reductions (0, 30, 60, and 80%) in $\tau_{O,d}$ and $\tau_{I,d}$ in NDMAR-Ab basal model relative to the Control model. P_3^r and P_{Ctrl}^r are related to NMDAR-Ab model #3 and Control model (Figure 6D), respectively. Intuitively, M_j^r quantifies the amount change in excessive θ- and γ-oscillatory powers arising from the reduced $\varepsilon_{SC,E}$. Note that the denominator of M_j^r is positive for both θ- and γ-oscillations. By this definition, $M_j^r = -1$ represents a full (i.e., 100%) suppression of the excessive power, bringing it back to the Control-model level. A M_j^r with values of 0 and >0 indicate no modulation and an increase of (i.e., deliberating) the excessive power, respectively. Peak powers were computed based on the power spectrums in the corresponding frequency bands.

QUANTIFICATION AND STATISTICAL ANALYSIS

Statistical analyses were performed using OriginPro 2019, MATLAB 2020a, and SPSS 27. All data are reported as mean ± standard error of the mean (SEM), if not stated otherwise. The Shapiro–Wilk test was used to test for normality. The F-test was used to test for homogeneity of variances. Parametric testing procedures were applied for normally distributed data; otherwise, nonparametric tests were used. Except for the Shapiro–Wilk test and F-test where p values <0.05 were considered statistically significant, the actual p values were stated for other tests. Bin-wise permutation tests in Figures 5E, 5I, S1D, S7A, S7C, and S7D were performed at a significance level of 5% adapting two-tailed permutation test of Cohen thereby accounting for multiple comparison problem (see STAR Methods for detail); the significant bins were designated by a star symbol. Whole-curve permutation tests (Figures 1I, 1M, 3F, S1J, S1K, and S4A) were performed by computing the area-under-curve (AUC) of the group-averaged curve, followed by computing the difference of AUCs of the two groups (empirical-difference; eDiff). The individual curves were then shuffled across the groups and the difference was re-calculated (shuffled-difference; sDiff). This was repeated for two million times. Finally, the p value (two-tailed) for eDiff was computed as the number of times that sDiff was bigger than |eDiff| or smallaer than -|eDiff|, divided by the number of shuffling times. Details of the applied statistical tests with the sample sizes are provided in Table S1.